
Fluid-structure coupling of linear elastic model with compressible flow models

Michael Herty¹, Siegfried Müller^{1,*}, Nils Gerhard¹,
Gaoming Xiang² and Bing Wang²

Institut für Geometrie und Praktische Mathematik
Templergraben 55, 52062 Aachen, Germany

¹ Institut für Geometrie und Praktische Mathematik, RWTH Aachen, Templergraben 55, 52056 Aachen, Germany.

² School of Aerospace Engineering, Tsinghua University, 100084, Beijing, China

* Corresponding author.

Email addresses:

herty@igpm.rwth-aachen.de (M. Herty), gerhard@igpm.rwth-aachen.de (N. Gerhard), mueller@igpm.rwth-aachen.de (S. Müller), xgm15@mails.tsinghua.edu.cn (G.M. Xiang), wbing@tsinghua.edu.cn (B. Wang).

Fluid-structure coupling of linear elastic model with compressible flow models

Michael Herty¹, Siegfried Müller^{1,*}, Nils Gerhard¹, Gaoming Xiang²
and Bing Wang²

¹ *Institut für Geometrie und Praktische Mathematik, RWTH Aachen, Templergraben
55, 52056 Aachen, Germany.*

² *School of Aerospace Engineering, Tsinghua University, 100084, Beijing, China*

Abstract. A novel coupling strategy for the simulation of fluid-structure interactions is introduced. The strategy is motivated by recent work on coupling of flows on networks. Here the novelty is to use an explicit approach rather than an implicit approach that avoids costly nested iterations where the fluid solver and the solid solver are called alternately. This concept is exemplified for the coupling of a linear elastic structure with an ideal gas. The coupling procedure relies on the solution of a nonlinear equation. Existence and uniqueness of the solution is proven. The coupling conditions are validated by means of quasi-1D problems for which an explicit solution can be determined. For a more realistic scenario a 2D application is considered where a hot gas bubble at low pressure collapses in a cold gas at high pressure near an adjacent structure.

AMS subject classifications: 74Q15, 76G25, 35Q30

Key words: Fluid-structure interaction; coupling conditions, linear elastic model, compressible flow.

1 Introduction

We are interested in the numerical and analytical treatment of fluid-structure interactions. More precisely, we study the coupling of material models with compressible fluid models. In particular, we apply the linear elasticity equations on the material side and the Euler equations for the fluid model. From continuum mechanics it is well-known that at the interface the stress tensor of the material model has to equal the pressure of the fluid and the displacement and velocity in normal direction should coincide, see [5], Chap. 5.1. This set of equations, the so-called transition conditions, couple the dynamics of the fluid and the material. The accurate resolution of the coupled dynamics poses a relevant problem for many industrial and engineering applications, e.g., fluid-structure interactions at airplane wings [2, 21].

A typical approach today is to iterate on the coupling condition until they are satisfied up to a prescribed tolerance before moving to the next time step. In the literature there are different coupling strategies discussed concerning their embedding into numerical methods. These differ in the discretization of the transition conditions and their incorporation into the simultaneous or alternating application of the two solvers discretizing the fluid system and structure system, respectively. A recent review can be found in [18]. In case of a strong coupling the approximations of both the fluid and the structure are updated simultaneously within one time step by a monolithic solver including the complete transition conditions without any splitting technique. Opposite to this, the basic idea

*Corresponding author. *Email addresses:* herty@igpm.rwth-aachen.de (M. Herty), gerhard@igpm.rwth-aachen.de (N. Gerhard), mueller@igpm.rwth-aachen.de (S. Müller), xgm15@mails.tsinghua.edu.cn (G.M. Xiang), wbing@tsinghua.edu.cn (B. Wang).

of weak coupling strategies, also known as partitioned approach or Gauss-Seidel method, consists of the alternating application of two separate solvers for the fluid and for the solid, respectively, where each solver uses boundary values provided by the other solver, see Figure 1 (right). Both the weak and the strong coupling strategy are global in the sense that they require an update of the entire flow field within each iteration step. This procedure is typically computationally expensive.

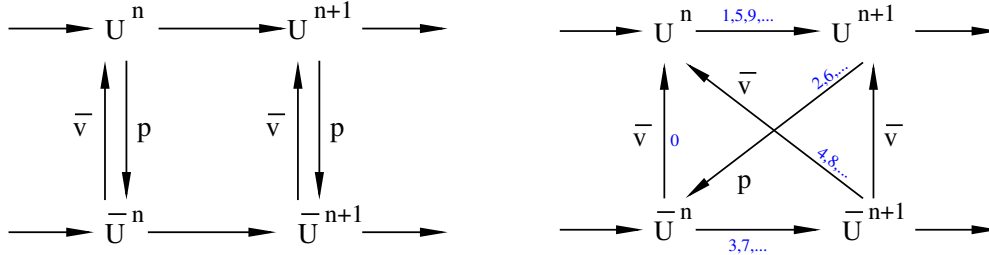


Figure 1: Illustration of explicit coupling (left) and weak coupling (right). n denotes the time step and \bar{v}, p denotes the variables appearing in the transition condition. The blue numbers denote the iterations required for updating the flow field. The variables U refer to the gas and \bar{U} to the material, respectively.

Inspired by recent results [6] on coupling of hyperbolic transport dynamics on networks we want to present a novel way for an explicit coupling of the dynamics. The main difference to classical approaches is to perform the coupling locally for each point on the interface *independent* from the other points and, thus, can be easily and efficiently parallelized. In particular, our strategy does not require an update of the entire flow field because a global iteration is avoided, see Figure 1 (left). The transition conditions will be reformulated such that the interface problem is equivalent to find the solution to a (scalar) nonlinear equation. Computationally, this is attractive, since it also resolves the dynamics locally very efficiently. We prove that the nonlinear equation admits a unique solution and that the arising boundary conditions for the material model as well as the fluid model are well posed. Numerical results highlighting this procedure will be discussed, too.

2 Description of the model problem

We consider a situation as in Figure 2 where an interface separates a material and a compressible gas. For simplicity we will not discuss moving interfaces. It is assumed that the interface remains unaffected by the interaction of material and gas flow. This is for example the case in [11]. Further, we assume that the material properties are sufficiently described by a linear elastic model (2.1):

$$\frac{\partial \bar{v}}{\partial t} - \frac{1}{\bar{\rho}} \nabla \cdot \bar{\sigma} = \mathbf{0}, \quad (2.1a)$$

$$\frac{\partial \bar{\sigma}}{\partial t} - \bar{\lambda} (\nabla \cdot \bar{v}) \mathbf{I} - \bar{\mu} (\nabla \bar{v} + \nabla \bar{v}^T) = \mathbf{0}. \quad (2.1b)$$

Here, the density of the material is denoted by $\bar{\rho}$ and assumed to be constant. The deformation velocities are $\bar{v} = (\bar{v}_1, \dots, \bar{v}_d)^T$, the stress tensor is denoted by $\bar{\sigma} = (\bar{\sigma}_{ij})_{i,j=1,\dots,d} = \bar{\sigma}^T$, and the Lamé constants are $\bar{\lambda}, \bar{\mu} > 0$. Further, the dilatation wave velocity and the shear wave velocity are $\bar{c}_1^2 := (2\bar{\mu} + \bar{\lambda})/\bar{\rho}$ and $\bar{c}_2^2 := \bar{\mu}/\bar{\rho}$, respectively. The system (2.1) is invariant under rotation and reflection. Due to the symmetry of the stress tensor $\bar{\sigma}$, the system of equations (2.1) contains redundant equations. Those may be removed and the system can be written in the canonical form of a system of conservation laws, see (A.1) in Appendix A.

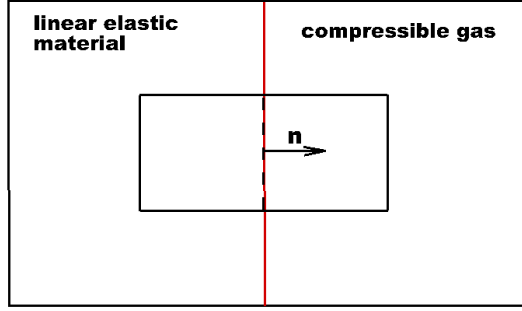


Figure 2: A sketch of the 2D problem with elastic material on the left and compressible gas on the right. Shown is the interface with its normal direction \mathbf{n} and two discretization cells aligned with the interface. The coupling of the dynamics will be across the interface in normal direction.

In the compressible gas regime we assume that the dynamics are governed by the Euler equations

$$\frac{\partial \rho}{\partial t} + \nabla \cdot (\rho \mathbf{v}) = 0, \quad (2.2a)$$

$$\frac{\partial \rho \mathbf{v}}{\partial t} + \nabla \cdot (\rho \mathbf{v} \mathbf{v}^T + p \mathbf{I}) = 0, \quad (2.2b)$$

$$\frac{\partial \rho E}{\partial t} + \nabla \cdot (\rho \mathbf{v} (E + p/\rho)) = 0, \quad (2.2c)$$

where we use the notation ρ for the gas density, $\mathbf{v} = (v_1, \dots, v_d)^T$, for its velocity, E for the total energy $E = e + 0.5\mathbf{v}^2$, pressure p and internal energy e . The system is not closed and an equation of state is required for a complete description, see [10, 20]. In the case of a perfect gas we have

$$p = (\gamma - 1)\rho e \quad (2.3)$$

and the speed of sound is given by

$$c = \sqrt{\frac{\gamma p}{\rho}}. \quad (2.4)$$

Here γ denotes the ratio of specific heat capacities that is assumed to be constant. In our computations we always use $\gamma = 1.4$ (air). Again, the system is invariant under rotation and reflection.

Across the interface we want to couple the gas dynamics to the material model. To this end we project the equation onto the normal direction \mathbf{n} of the interface. For notational convenience we assume the normal direction $\mathbf{n} = (n_i)_{i=1}^d$ pointing from the material towards the gas regime. We project the linear elasticity model in $d \in \{1, 2, 3\}$ spatial dimensions onto direction $\mathbf{n} \in \mathbb{R}^d$ and obtain a quasi-1D model in the normal direction $x_n := \mathbf{n} \cdot \mathbf{x}$

$$\frac{\partial \bar{\mathbf{u}}}{\partial t} + \frac{\partial \bar{\mathbf{f}}_n(\bar{\mathbf{u}})}{\partial x_n} = \mathbf{0}, \quad (2.5a)$$

$$\bar{\mathbf{f}}_n(\bar{\mathbf{u}}) := \sum_{i=1}^d \bar{\mathbf{f}}_i(\bar{\mathbf{u}}) n_i. \quad (2.5b)$$

Here $\bar{\mathbf{u}}$ and $\bar{\mathbf{f}}_i$ are defined by (A.1) in Appendix A. The eigenvalues of the projected system (2.5), see (A.8), (A.9) and (A.10) in Appendix A are independent of the direction \mathbf{n} .

Similarly, we project the gas equations onto \mathbf{n} . Provided there is no flow of gas in tangential

directions $\tilde{x}_{i+1} = \mathbf{x} \cdot \mathbf{t}_i$, $i = 1, \dots, d-1$, the system (2.2) reduces to the projected system:

$$\frac{\partial \tilde{\mathbf{u}}}{\partial t} + \frac{\partial \mathbf{f}_n(\tilde{\mathbf{u}})}{\partial x_n} = \mathbf{0}, \quad (2.6a)$$

$$\tilde{\mathbf{u}} := (\rho, \rho \tilde{\mathbf{v}}, \rho E)^T, \quad \tilde{\mathbf{v}} := (\mathbf{n} \cdot \mathbf{v}, \mathbf{t}_1 \cdot \mathbf{v}, \dots, \mathbf{t}_{d-1} \cdot \mathbf{v})^T, \quad v_n := \mathbf{n} \cdot \mathbf{v}, \quad (2.6b)$$

$$\mathbf{f}_n(\tilde{\mathbf{u}}) := \sum_{i=1}^d \mathbf{f}_i(\tilde{\mathbf{u}}) n_i = \begin{pmatrix} \rho v_n \\ \rho v_n \tilde{\mathbf{v}} + p \mathbf{n} \\ \rho v_n (E + p/\rho) \end{pmatrix}, \quad (2.6c)$$

where \mathbf{f}_i is defined by (B.1b) in Appendix B. Since both systems (2.5) and (2.6) are invariant under rotation and reflection, we consider only the projection into direction $\mathbf{n} = \mathbf{e}_1 = (1, 0, \dots, 0)^T \in \mathbb{R}^d$, see Figure 2.

The basic problem is now to couple the projected systems at the interface located for simplicity at the point $x_n = 0$. Then, the projected linear elastic model is defined for $x_n < 0$ and the projected Euler equations for $x_n > 0$. The coupling of hyperbolic models has been discussed analytically and numerically in many recent publications and we refer to [6] for a survey. Particular results for the coupling of Euler equations with Euler equations exist and have been studied e.g. in [9]. Numerical approaches have been proposed e.g. in [3, 14]. Coupling the dynamic requires to postulate conditions to be fulfilled at the interface $x_n = 0$ for a.e. $t \geq 0$. Depending on the coupling conditions different wave patterns might be observed [4].

According to the transition conditions of continuum mechanics at a material interface we model the coupling by requiring the following conditions to be fulfilled at $x_n = 0$:

$$\mathbf{n}^T \bar{\boldsymbol{\sigma}} \mathbf{n} \equiv \bar{\sigma}_{nn} \stackrel{!}{=} -p, \quad (2.7a)$$

$$\bar{\mathbf{v}}^T \mathbf{n} \equiv \bar{v}_n \stackrel{!}{=} v_n \equiv \mathbf{v}^T \mathbf{n}, \quad (2.7b)$$

neglecting viscosity and heat conduction in the gas flow. These are referred to as transition and kinematic or coupling conditions, respectively. In the following section we show that the coupling conditions (2.7) are well-posed and in fact impose suitable boundary conditions for the material and the gas flow domain. The conditions are still written in the general formulation but due to the rotational invariance we only consider the coupling in x_n -direction, i.e., $\mathbf{n} = \mathbf{e}_1$. The conditions prescribe an equal stress and pressure at the interface. This is due to the analogy of $\bar{\boldsymbol{\sigma}}$ in material models and the effect of pressure p in compressible flow models. Also, we assume that across the interface the velocities are equal. Therefore, we model a stationary interface.

Remark 2.1. Subsequently the procedure to obtain boundary conditions will be described for normal directions equal to the unit vector. However, due to the rotational invariance the same can be enforced across any direction $\mathbf{n}_{\bar{\Gamma}}$. In this case we therefore suggest the following procedure. Assume states $\bar{\mathbf{u}}_L$ (material) and \mathbf{u}_R (fluid) are given.

1. Project the states of the structure and the fluid by means of the corresponding rotation matrices \mathbf{G} , \mathbf{R} (see Appendix A, B). $\tilde{\bar{\mathbf{u}}}_L = \mathbf{G} \bar{\mathbf{u}}_L$ and $\tilde{\mathbf{u}}_R = \mathbf{R} \mathbf{u}_R$
2. Evaluate the coupling conditions (2.7) providing the states $\tilde{\bar{\mathbf{u}}}$ (material) and $\tilde{\mathbf{u}}$ (fluid) at the interface.
3. Project the states of the material and the fluid back to the original normal direction \mathbf{n} by means of $\bar{\mathbf{u}} = \mathbf{G}^{-1} \tilde{\bar{\mathbf{u}}}$ and $\mathbf{u} = \mathbf{R}^T \tilde{\mathbf{u}}$.

If the material is to the right of the fluid we have to switch the sign in the normal velocity, perform coupling and finally, switch back the sign of the normal velocity in the states determined at the interface. The main focus will now be on the resolution of the coupling itself, i.e., Step 2.

3 Well-posedness on the coupling conditions

The coupling conditions (2.7) impose boundary conditions at $x_n = 0$ on the material as well as on the fluid side. This section is devoted to the understanding of the well-posedness of the boundary conditions obtained through the coupling. A general result for coupling of the *same* spatially one-dimensional conservation law has been presented e.g. in [8]. The coupling of different *scalar* conservation laws has been discussed also in [17]. Further references and an application of those techniques to other models can be found e.g. in [6] and e.g. in [14–16] and [1].

3.1 Admissible boundary states on the material side

On the material side the governing system is given by equation (2.5). The system is a linear strictly hyperbolic system and therefore the characteristic velocities are constant, see (A.8), (A.9) and (A.10) in Appendix A. For typical material parameters $\bar{\rho} > 0, \bar{c}_1, \bar{c}_2 > 0$ we have negative, positive and zero eigenvalues. More precisely, for the projected system and in the case of one spatial dimension ($d = 1$) we have a single negative and a single positive eigenvalue, see Figure 3 (left). For $d = 2$, we have two negative, two positive and a zero eigenvalue. For $d = 3$ we have three negative (two coinciding), three positive (two coinciding) and three zero eigenvalues, see Figure 3 (right). The algebraic and geometric multiplicity are equal. All fields are contact discontinuities. The characteristic fields related to the zero eigenvalues have the following property: across this characteristic field the velocities $\bar{v}_i, i = 1, \dots, d$, and stresses $\bar{\sigma}_{ij}$ for $i = 1$ and $j = 1, \dots, d$ are constant. For more details we refer to Appendix A.

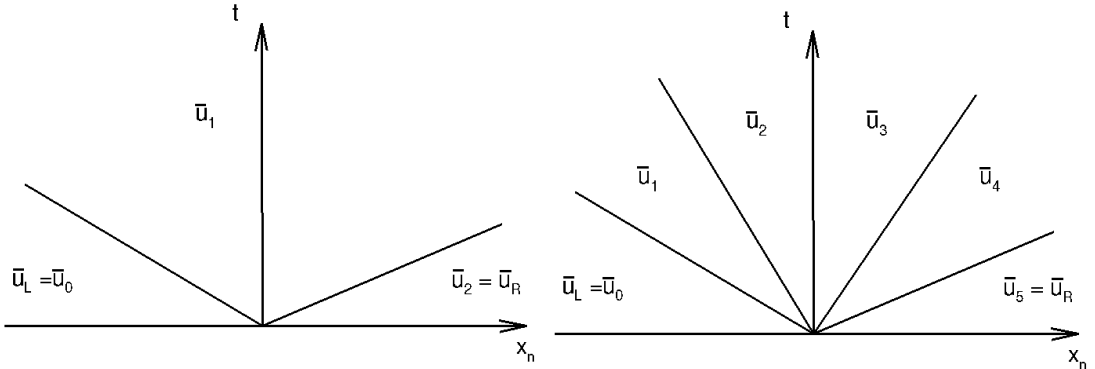


Figure 3: Riemann problem for projected linear elastic system in the case $d = 1$ (left) and $d \geq 2$ (right).

Due to the characteristic velocities we may prescribe a single boundary condition at $x_n = 0$ along the fields associated to the eigenvalues of negative sign. Since for $d = 3$ the fields coincide we have two degrees of freedom at the boundary $x_n = 0$. For a given state $\bar{\mathbf{u}}$, the states $\bar{\mathbf{v}}$ that can be connected by a single, self-similar wave of the k th family are given by

$$\mathbf{v}(\epsilon) = \bar{\mathbf{u}} - (\epsilon - \bar{\lambda}_k) \bar{\mathbf{r}}_k,$$

for any $\epsilon \in \mathbb{R}$. Here, $\bar{\lambda}_k$ denotes the constant k th eigenvalue and $\bar{\mathbf{r}}_k$ the corresponding normalized right eigenvector of the Jacobian see (A.11), (A.12) and (A.13) in Appendix A. The states $\mathbf{v}(\epsilon)$ are the k th Lax-curve $\bar{L}_k^+(\epsilon; \bar{\mathbf{u}})$ emanating from a state $\bar{\mathbf{u}}$. In the case $d = 1, \dots, 3$, we therefore obtain the set of all possible boundary states for the projected system and given state \bar{u}_L as

$$\bar{V} := \left\{ \bar{\mathbf{v}}(\epsilon_1, \dots, \epsilon_d) : \bar{\mathbf{v}}(\epsilon_1, \dots, \epsilon_d) = \bar{\mathbf{u}}_L + (\epsilon_1 - \bar{\lambda}_1) \bar{\mathbf{r}}_1 + \sum_{i=2}^d (\epsilon_i - \bar{\lambda}_2) \bar{\mathbf{r}}_i : \forall \epsilon_j \in \mathbb{R} \right\}$$

where we suppose that the eigenvalues are ordered in increasing order and denote by $\bar{\mathbf{r}}_i$ the corresponding eigenvector. Across the characteristic field related to the zero eigenvalue the velocities and stresses are constant. In view of the coupling condition (2.7) those waves cannot be used to describe the admissible boundary states.

In order to evaluate the coupling condition (2.7) we require the stress σ_{11} and velocity v_1 in direction $\mathbf{n} = \mathbf{e}_1$ to be elements of the set \bar{V} , i.e., for all d and a given state $\bar{\mathbf{u}}_L$,

$$\bar{\sigma}_{11}(\epsilon_1, \dots, \epsilon_d) = \bar{\sigma}_{11,L} + (\epsilon_1 - \bar{\lambda}_1) \bar{\rho} \bar{c}_1 \bar{\beta}(d), \quad (3.1a)$$

$$\bar{v}_1(\epsilon_1, \dots, \epsilon_d) = \bar{v}_{1,L} + (\epsilon_1 - \bar{\lambda}_1) \bar{\beta}(d), \quad (3.1b)$$

where according to Appendix A β is a constant depending only on d :

$$\bar{\beta}(1) = 1, \quad \bar{\beta}(2) = \bar{c}_1^2 - \bar{c}_2^2, \quad \bar{\beta}(3) = -1/(\bar{\rho} \bar{c}_1). \quad (3.2)$$

Hence, due to the eigenspaces of the projected system there is only a single degree of freedom for determining boundary values for projected linear elasticity equations.

3.2 Admissible boundary states on the gas side

In the domain $x_n > 0$ we consider the projected Euler equations. In the general case $d \geq 1$, the eigenvalues at state \mathbf{u} are $\lambda_1(\mathbf{u}) = v_n - c$, $\lambda_i(\mathbf{u}) = v_n$, $i=2, \dots, d+1$, and $\lambda_{d+2}(\mathbf{u}) = v_n + c$ where the sound speed c is given by equation (2.4). The characteristic fields associated with the eigenvalues v_n are linearly degenerated and lead to contact discontinuities. Across the contact discontinuities the normal velocity v_n is preserved as well as the pressure p .

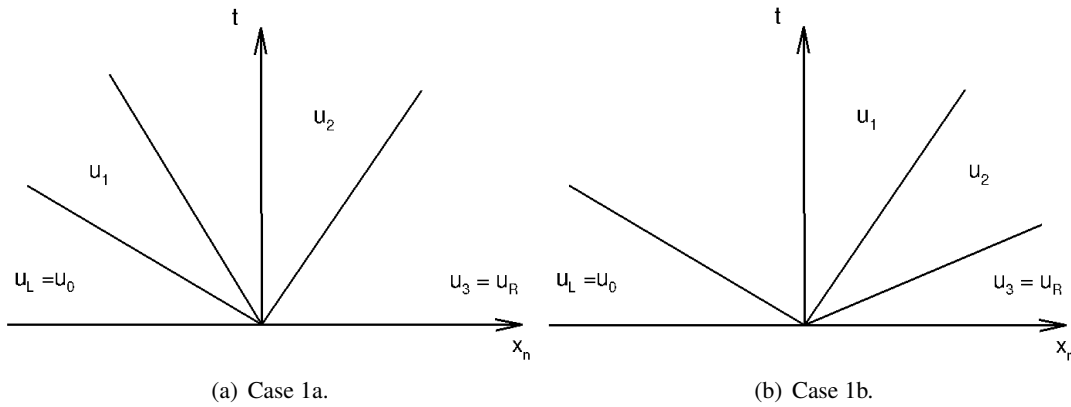


Figure 4: Riemann problem for projected Euler system and in the case of subsonic initial data.

The other two fields are genuinely nonlinear. Since the sign of the eigenvalues depend on the state of the system, the number of boundary conditions depends on the normal velocity relative to the sound speed c of the state \mathbf{u} . As in [6] we assume that the given state \mathbf{u} is subsonic, i.e.,

$$\lambda_1(\mathbf{u}) < 0 < \lambda_{d+2}(\mathbf{u}) \quad \text{or, equivalently,} \quad \frac{|v_n|}{c} < 1. \quad (3.3)$$

In this case we have at least one degree of freedom at the boundary according to the $(d+2)$ -characteristic field. Note that the proposed coupling condition is stated in terms of the pressure p as well as the normal velocity v_n . Those are constant across contact discontinuities. Assume a given subsonic state \mathbf{u}_R . Possible boundary states that can be connected by simple waves to \mathbf{u}_R are obtained through the reversed $(d+2)$ -Lax-curve parameterized by $\epsilon \in \mathbb{R}$ and denoted by

$\mathbf{L}_{d+2}^-(\epsilon; \mathbf{u}_R)$. We choose the parameterization of the Lax-curve such that $\mathbf{L}_{d+2}^-(0; \mathbf{u}_R) = \mathbf{u}_R$ and refer to equations (B.7) and (B.8) in Appendix B in the case $d = 1$. For $d = 2, 3$ the tangential velocities have to be added that are constant along the $(d+2)$ -characteristic curve. Note that we choose the reversed Lax-curve, since for a Riemann problem we have the right initial datum given and need to connect it to a state on the left. In order to prevent a sonic transition by this construction, the value of ϵ has to be sufficiently small. Note that we cannot connect through any wave of the characteristic families $i = 2, \dots, d+1$, since those waves do not change the pressure and normal velocity but the density and the tangential velocities. Summarizing, the possible boundary states for the projected Euler system and a given state \mathbf{u}_R are

$$V := \left\{ \mathbf{v}(\epsilon) : \mathbf{v}(\epsilon) = \mathbf{L}_{d+2}^-(\epsilon; \mathbf{u}_R), \forall \epsilon \in \mathbb{R} \text{ such that } \lambda_1(\mathbf{v}(\epsilon)) < 0 < \lambda_2(\mathbf{v}(\epsilon)) \right\}.$$

Due to the continuity of the Lax curves [10] the previous set is non-empty.

3.3 Analytical results on strong coupling

In order to obtain boundary conditions for the linear elastic model and the gas model, respectively, we solve (2.7). Given the current state $\bar{\mathbf{u}}_L$ of the linear elastic model and the state \mathbf{u}_R of the Euler equations we solve for values $\bar{\sigma}_{nn} \equiv \bar{\sigma}_{11}$, $\bar{v}_n \equiv \bar{v}_1$ out of the set \bar{V} and $p, v_n \equiv v_1$ in the set V , i.e., this amounts to solve the following nonlinear set of equations for the parameters ϵ_1 and ϵ

$$\bar{\sigma}_{11}(\epsilon_1) \stackrel{!}{=} -p(\epsilon), \bar{v}_1(\epsilon_1) \stackrel{!}{=} v_1(\epsilon). \quad (3.4)$$

The precise formulas for p, v_1 are obtained from the states computed along the reverse Lax-curve $\mathbf{L}_{d+2}^-(\epsilon; \mathbf{u}_R)$. Provided the previous nonlinear system has a unique solution $(\epsilon_1^*, \epsilon^*)$, with ϵ^* sufficiently small, the boundary conditions are given by

$$\bar{\mathbf{U}}_R := \bar{\mathbf{u}}_L + (\epsilon_1^* - \bar{\lambda}_1) \bar{\mathbf{r}}_1$$

at $x_n = 0-$ for the linear elastic model and

$$\mathbf{U}_L := \mathbf{L}_{d+2}^-(\epsilon^*; \mathbf{u}_R)$$

at $x_n = 0+$ for the Euler equations, see Figure 5. Note that there might be additional terms for the fluid and the elastic material ($d \geq 2$) that do not change the coupling conditions. Numerically, the system of nonlinear equations is solved using Newton's method. Due to the parameterization a possible initial guess for Newton's method is $\epsilon_1 = \epsilon = 0$.

Due to the construction the waves emanating from the boundary will move into each respective domain. Also, for small $t > 0$ the coupling condition is fulfilled at x_n by construction. It remains to prove the existence of a unique solution to equation (3.4). The given states are $\bar{\mathbf{u}}_L$ and \mathbf{u}_R , respectively. For readability we denote by $\bar{\xi} = (\epsilon_1 - \bar{\lambda}_1)$ the parameterization of the Lax curve in the linear elastic system and by $\sigma \equiv \epsilon$ the parameterization of the reversed Lax curve for the Euler system. Then, condition (3.4) reads

$$\bar{\sigma}_{11,L} + \bar{\xi} \bar{\rho} \bar{c}_1 \bar{\beta} = -p(\sigma), \quad (3.5a)$$

$$\bar{v}_{1,L} + \bar{\xi} \bar{\beta} = v_1(\sigma) \quad (3.5b)$$

with $\bar{\beta} = \bar{\beta}(d)$ determined by (3.2). This is equivalent to

$$g(\sigma) := \bar{\sigma}_{11,L} + \bar{\rho} \bar{c}_1 (v_1(\sigma) - \bar{v}_{1,L}) + p(\sigma) = 0, \quad (3.6a)$$

$$\bar{\xi} = (v_1(\sigma) - \bar{v}_{1,L}) \frac{1}{\bar{\beta}}. \quad (3.6b)$$

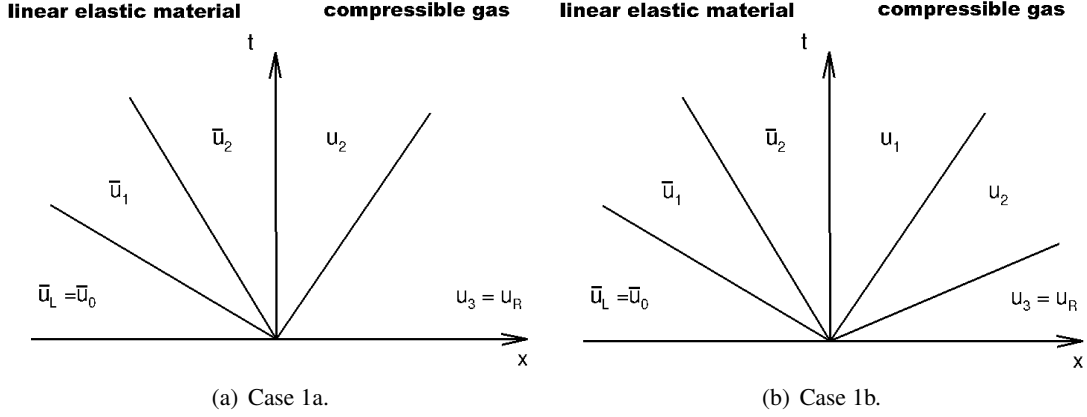


Figure 5: Coupling of linear elastic system (left) and Euler system (right) for $d \geq 2$: Subsonic cases. Note that for $d = 1$ there exists only one wave in the elastic material.

Note that the function g is dependent on the spatial dimension d only through $\beta(d)$, that is a constant. Further, σ has to be sufficiently small to guarantee the subsonic condition on the boundary states for the Euler equation. The reversed Lax-curve \mathbf{L}_{d+2}^- for the $(d+2)$ -family is determined by (B.7) and (B.8) in Appendix B. Note that the states ρ , $v \equiv v_1$ and e along these curves are the same for all $d = 1, 2, 3$. Therefore, the function g in (3.6) is given by the corresponding backward shock curve ($\sigma \leq 0$)

$$g(\sigma) = \bar{\sigma}_{11}^L + \bar{\rho}\bar{c}_1 \left(v_R + \sqrt{\frac{2}{(2\rho_R + (\gamma-1)\sigma)(\rho_R - \sigma)}} |\sigma| c_R - \bar{v}_1^L \right) + \frac{1}{\gamma} \frac{2\rho_R - (\gamma+1)\sigma}{2\rho_R + (\gamma-1)\sigma} \rho_R c_R^2 \quad (3.7)$$

and rarefaction curve ($\sigma \geq 0$)

$$g(\sigma) = \bar{\sigma}_{11}^L + \bar{\rho}\bar{c}_1 \left(v_R - \frac{2}{\gamma-1} \left(1 - \left(1 - \frac{\sigma}{\rho_R} \right)^{(\gamma-1)/2} \right) c_R - \bar{v}_1^L \right) + (\gamma-1) e^{s_R/c_v} (\rho_R - \sigma)^\gamma, \quad (3.8)$$

respectively. Here we use $c^2(\rho, e) = \gamma(\gamma-1)e$ derived from (2.3) and (2.4). Furthermore, s is the entropy. For a perfect gas the relation is as follows: $e(\rho, s) = e^{s/c_v} \rho^{\gamma-1}$, where $\gamma = c_p/c_v$ with c_v and c_p the specific heat capacities at constant volume and pressure, respectively. The subindex R refers to those quantities related to the given datum \mathbf{u}_R . The parameters $\bar{\rho}$ and \bar{c}_1 are the constant density and dilatation wave velocity, respectively, of the elastic material. Due to the C^2 -connection at $\sigma = 0$ of the reversed Lax-curve the function g is differentiable even at $\sigma = 0$. The next lemma discusses monotonicity properties of g as a function of σ .

Lemma 3.1. *Let be $\gamma > 1$ and $\rho_R, p_R, \bar{\rho}, \bar{c}_1 > 0$. Then for a perfect gas the function $g: (\sigma_m, \sigma_M] \rightarrow \mathbb{R}$ consisting of the shock branch (3.7) and the rarefaction branch (3.8) is differentiable and strictly monotonically decreasing.*

Proof. The shock branch ($\sigma \leq 0$) is well-defined as long as the discriminant in (3.7) is positive, i.e.,

$$\sigma_m := -\frac{2\rho_R}{\gamma-1} < 0.$$

The rarefaction branch ($\sigma \geq 0$) is well-defined provided that the term $(\rho_R - \sigma)^{(\gamma-1)/2}$ is well-defined. For this purpose we have to distinguish between two cases

$$\tilde{\sigma}_M := \begin{cases} \infty & , \quad (\gamma-1)/2 \in \mathbb{N} \\ \rho_R & , \quad (\gamma-1)/2 \in (1, \infty] \setminus \mathbb{N} \end{cases} .$$

Therefore, each branch of the function g is differentiable with derivatives of the shock branch ($\sigma_m < \sigma \leq 0$) and of the rarefaction branch ($0 \leq \sigma \leq \tilde{\sigma}_M$) given by

$$g'(\sigma) = \bar{\rho} \bar{c}_1 \sqrt{2} c_R \left(\frac{(\gamma-3)\rho_R \sigma - 2(\gamma-1)\sigma^2}{2[(2\rho_R + (\gamma-1)\sigma)(\rho_R - \sigma)]^{3/2}} - \frac{1}{\sqrt{(2\rho_R + (\gamma-1)\sigma)(\rho_R - \sigma)}} \right) - \frac{4\rho_R^2 c_R^2}{(2\rho_R + (\gamma-1)\sigma)^2}, \quad \sigma \leq 0, \quad (3.9)$$

$$g'(\sigma) = -\frac{\bar{\rho} \bar{c}_1 c_R}{\rho_R} \left(1 - \frac{\sigma}{\rho_R}\right)^{(\gamma-3)/2} - c_R^2 \left(1 - \frac{\sigma}{\rho_R}\right)^{\gamma-1}, \quad \sigma \geq 0. \quad (3.10)$$

The function g is continuously differentiable at $\sigma=0$ because

$$\begin{aligned} g(0^-) &= g(0^+) = \bar{\sigma}_{11}^L + \bar{\rho} \bar{c}_1 (v_R - \bar{v}_1^L) + \rho_R c_R^2 / \gamma, \\ g'(0^-) &= g'(0^+) = -(\bar{\rho} \bar{c}_1 + \rho_R c_R) c_R / \rho_R < 0. \end{aligned}$$

Along the shock branch ($\sigma_m < \sigma \leq 0$) the function g is strictly monotonically decreasing. According to (3.9) this holds true if

$$(\gamma-3)\rho_R \sigma - 2(\gamma-1)\sigma^2 - 2(2\rho_R + (\gamma-1)\sigma)(\rho_R - \sigma) \leq 2\sqrt{2} \frac{\rho_R^2 c_R}{\bar{\rho} \bar{c}_1} \sqrt{\frac{(\rho_R - \sigma)^3}{2\rho_R + (\gamma-1)\sigma}}$$

Since the left-hand side reduces to $-4\rho_R^2 + \rho_R \sigma (\gamma+3)$ that is negative along the shock branch and the right-hand side is positive, this inequality is satisfied. For the rarefaction branch ($0 \leq \sigma \leq \tilde{\sigma}_M$) we obtain by (3.10)

$$g'(\sigma) = -c_R^2 \rho_R^{-2r} \left(\alpha (\rho_r - \sigma)^{r-1} + (\rho_r - \sigma)^{2r} \right)$$

with $\alpha := c_R^{-1} \rho_R^r \bar{\rho} \bar{c}_1 > 0$ and $r := (\gamma-1)/2$. Obviously, g' has one root in ρ_R . If $r \notin \mathbb{N}$ or $r \in \mathbb{N}$ is odd, then g' is negative for $\sigma \in [0, \sigma_M)$. However, if $r \in \mathbb{N}$ is even, then g' is positive if

$$\rho_R < \sigma < \rho_R + \alpha^{2/(\gamma+1)}.$$

Hence, g is strictly monotonically decreasing if σ does not exceed

$$\sigma_M := \begin{cases} \infty & , \quad (\gamma-1)/2 \in \mathbb{N}, \text{ odd} \\ \rho_R & , \quad (\gamma-1)/2 \in (1, \infty] \setminus \mathbb{N} \text{ or } (\gamma-1)/2 \in \mathbb{N}, \text{ even} \end{cases}$$

This finishes the proof. \square

The monotonicity of g can be used to prove the existence of unique states $(\bar{\zeta}^*, \sigma^*)$ fulfilling the coupling condition (3.6).

Theorem 3.1. *Let be $\gamma > 1$ and $\rho_R, p_R, \bar{\rho}, \bar{c}_1 > 0$. Then for a perfect gas there exists a unique root of the function $g: (\sigma_m, \sigma_M] \rightarrow \mathbb{R}$ and, thus a unique solution $(\bar{\zeta}^*, \sigma^*)$ of the coupling condition (3.6), respectively, provided that the initial data $(\bar{v}_1^L, \bar{\sigma}_{11}^L)$ and (ρ_R, v_R, p_R) satisfy*

$$v_R \leq \frac{2}{\gamma-1} c_R + \bar{v}_1^L - \frac{\bar{\sigma}_{11}^L}{\bar{\rho} \bar{c}_1} \quad (3.11)$$

in case of $(\gamma-1)/2 \in (1, \infty] \setminus \mathbb{N}$ or $(\gamma-1)/2 \in \mathbb{N}$ even.

Proof. For σ approaching σ_m from the right we conclude from (3.7) that $\lim_{\sigma \rightarrow \infty} g(\rho) = \infty$. For $\sigma \geq 0$ we distinguish two cases. If $(\gamma-1)/2 \in (1, \infty) \setminus \mathbb{N}$ or $(\gamma-1)/2 \in \mathbb{N}$ even, then $\sigma_M = \rho_R$ and $g(\rho_R) \leq 0$ if

$$\bar{\sigma}_{11}^L + \bar{\rho} \bar{c}_1 \left(v_R - \frac{2}{\gamma-1} c_R - \bar{v}_1^L \right) \leq 0.$$

This inequality holds because of assumption (3.11). For the other case where $(\gamma-1)/2 \in \mathbb{N}$ odd, then $\sigma_M = \infty$ and $\lim_{\sigma \rightarrow \infty} g(\rho) = -\infty$. According to Lemma 3.1 the function g is strictly monotonically decreasing in $(\sigma_m, \sigma_M]$ and, thus, the assertion follows. \square

Note that we cannot guarantee with the previous theorem that the final state $\mathbf{U}_L = \mathbf{L}_{d+2}^-(\sigma^*; \mathbf{U}_R)$ is subsonic. However, in the numerical results we never observed a sonic transition in normal direction at the coupling interface.

Conclusion: 3.1. Let be $d=3, \gamma \in (1, 3)$ and $\rho_R, p_R, \bar{\rho}, \bar{c}_1 > 0$. Let the fluid state be subsonic, i.e., (3.3) holds. Then for a perfect gas a sufficient condition for a unique solution of the coupling condition (3.6) is

$$\bar{v}_{1,L} \geq \frac{\bar{\sigma}_{11,L}}{\bar{\rho} \bar{c}_1}. \quad (3.12)$$

Proof. The subsonic condition (3.3) implies $v_r \leq c_R < c_R \frac{2}{\gamma-1}$, $\gamma \in (1, 3)$. Together with (3.12) we conclude that the condition (3.11) is satisfied. \square

Remark 3.1. Similar results can be obtained in the case $d=1, 2$, respectively. The only change is the Lax curve for the Euler system. However, the monotonicity behavior is similar and the result is therefore omitted. Further, a similar result is true for coupling linear elasticity models with the p -system instead of the Euler system. We omit this simpler case. Further, the coupling of linear elasticity models with itself or Euler system with itself does yield the same solutions as a classical Riemann problem. We also omit the details here. Even so in practical applications only the cases 2D and 3D might be relevant, the result also holds in 1D as well as spatial dimensions larger than three.

4 Numerical results

In order to solve the coupled problem consisting of the linear elastic model and the compressible Euler equations we apply a Runge-Kutta discontinuous Galerkin (RK-DG) method [7] to each of the systems. Both solvers are connected at the material interface via weakly enforced boundary conditions, i.e., admissible (boundary) states are plugged into the (local) flux integrals on the boundary of the scheme. At the material interface these states are locally determined for each solver by solving the nonlinear problem (3.5) using states from both solvers. In the DG scheme these boundary integrals are computed with a suitable quadrature rule. Thus, the non-linear system is solved at each quadrature point independently. For that reason, both solvers require only *local* access to the DG solution of the other solver at the interface, respectively. For that reason, the coupling can be implemented very efficiently.

We apply on both sides a third order DG scheme using polynomial elements of order $p=3$ and a third-order SSP-Runge-Kutta method with three stages for the time-discretization. Both solvers have the same numerical flux and limiter, namely, the local Lax-Friedrichs flux, the minmod limiter from [7]. The time stepping of both solvers is synchronized, i.e., both solvers apply the same (minimal) timestep size determined by the same CFL number.

The performance is enhanced by local multi-resolution based grid adaptation, see [19]. Details on the adaptive solver can be found in [12, 13]. The grid adaptation of both solvers is intertwined,

i.e., if in one solver the grid near the material interface is refined, this refinement is communicated to the other solver and the grid of the other solver is refined as well.

For our computations we always choose plastics for the linear elastic material with density $\bar{\rho} = 1226 \text{ kg/m}^3$ and Lamé constants $\mu = 1.4093e9 \text{ N/m}^2$ and $\lambda = 1.4093e9 \text{ N/m}^2$. The corresponding dilatation wave velocity and shear wave velocity are $\bar{c}_1 = 1857.02 \text{ m/s}$ and $\bar{c}_2 = 1072.15 \text{ m/s}$, respectively. For the fluid we consider air. The corresponding material parameters for the ideal gas are chosen as $\gamma = 1.4$ and $c_v = 717.5 \text{ J/(kg}\cdot\text{K)}$.

4.1 (Quasi-)1D Validation

To validate the coupling conditions and their implementation we design (quasi-)1D test configurations that can explicitly construct the exact solution as sketched in Figure 6.

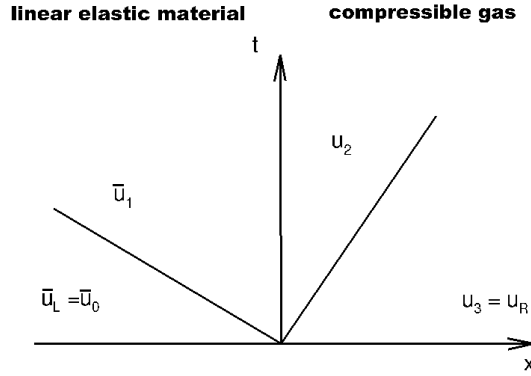


Figure 6: Setup for validation test case.

To determine appropriate initial states we proceed in three steps:

- We choose some values for the normal velocity component velocity v^* , the pressure p^* and the density ρ^* such that the corresponding Mach number $M^* = v^*/c(\rho^*, p^*)$ is subsonic. Furthermore, in the higher dimensional case, we also fix the stresses $\bar{\sigma}_{ij}^*$, $1 \leq i \leq j \leq d$, $i+j > 2$, the tangential velocities \bar{v}_i^* and v_i^* , $i = 2, \dots, d$. Then we set the fluid state

$$\rho_2 = \rho^*, \quad \mathbf{v}_2 = (v_1^*, v_2^*, \dots, v_d^*)^T, \quad p_2 = p^*$$

and the state in the linear elastic material

$$\bar{\mathbf{v}} = (v_1^*, \bar{v}_2^*, \dots, \bar{v}_d^*)^T, \quad \bar{\sigma}_{11} = -p^*, \quad \bar{\sigma}_{ij} = \bar{\sigma}_{ij}^*.$$

at the interface. Thus, we have fixed the state $\bar{\mathbf{u}}_1 = (\bar{v}_1, \bar{\sigma}_{11})^T$ in the elastic material and the state $\mathbf{u}_2 = (\rho_2, \rho_2 \mathbf{v}_2^T, \rho_2 (e(\rho_2, p_2) + 0.5 \mathbf{v}_2^2))^T$ in the fluid, see Figure 6.

- For the state $\bar{\mathbf{u}}_L$ in the elastic material we choose a state on the backward 1-Lax curve emanating from the state $\bar{\mathbf{u}}_1$, i.e.,

$$\bar{\mathbf{u}}_L = \bar{\mathbf{u}}_1 - (\zeta - \bar{\lambda}_{1,-}) \bar{\mathbf{r}}_{1,-} \quad (4.1)$$

where we fix the parameters $\zeta_i = \zeta_i^*$, $i = 1, \dots, d$.

- For the state \mathbf{u}_R in the gas we choose a state on the forward 3-Lax curve emanating from the state \mathbf{u}_2 , i.e.,

$$\mathbf{u}_R = \mathbf{L}_3^+(\eta; \mathbf{u}_2),$$

where we fix the parameter $\eta = \eta^*$ such that the corresponding Mach number $M_R = v^*/c(\rho_R, p_R)$ is subsonic.

- We solve the coupled problem with homogeneous states $\bar{\mathbf{u}}_L$ and \mathbf{u}_R in the elastic material (left) and the gas (right), respectively.

Since the states $\bar{\mathbf{u}}_L$ and \mathbf{u}_R satisfy the sufficient condition 3.11, then there exists a unique solution of the coupling conditions 3.5 according to Theorem 3.1. By construction the corresponding states at the interface determined from these unique parameters must coincide with the states $\bar{\mathbf{u}}_1$ and \mathbf{u}_2 . Thus, the solution of the problem must be the one shown in Figure 6. For the validation we perform computations in 1D and 2D, respectively. For initial data we have chosen two setups where the \mathbf{L}_3^+ -curve is always a shock wave.

In the following we present the validation only for the 1D case. We also performed a validation in 2D with planar waves. The results are similar and therefore omitted here. The computational domain is $\Omega \in [0,1] m$ for the linear elastic system and $\Omega \in [1,2] m$ for the Euler system. Each domain is discretized by $N_0 = 16 \times 2^L$ cells. The CFL number is set to 0.1 and the final time is $t = 0.0002s$. In each domain we set uniform initial data $\bar{\mathbf{u}}_L$ (linear elastic material) and \mathbf{u}_R (fluid) that are determined from the parameters

$$v^* = 1, \quad p^* = 200000, \quad \rho^* = 1.0, \quad \zeta_1 = 0.1$$

according to the above procedure. The data are listed in Table 1.

Elastic material			Fluid		
	$\bar{\mathbf{u}}_L$	$\bar{\mathbf{u}}_1$		\mathbf{u}_2	\mathbf{u}_R
$\bar{v}_1 [m/s]$	1.1	1	$v_1 [m/s]$	1	-355.8
$\bar{\sigma}_{11} [N/m^2]$	27668.2	-200000	$p [N/m^2]$	200000	72727.3
			$\rho [kg/m^3]$	1	0.5

Table 1: Initial data for 1D validation test case.

Note that the shock speed in the fluid corresponding to the initial data is about $s = 357.8 m/s$. This is about $1/5th$ of the dilatation wave velocity in the elastic material. We have performed several computations with increasing spatial and temporal resolution by a factor two with each additional refinement level. In Tables 2, 3 we summarize the error and the empirical order of convergence (EoC). Here the error is computed separately in the elastic material and the fluid where the L_1 -error is computed as $e_L := \int_{\Omega} |u_L(x) - u(x)| dx$ with u_L and u denoting the DG solution for refinement level L and the exact solution, respectively. From the error we compute $EoC = -\log_2(e_{L+1}/e_L)$. The computational results indicate grid convergence. To validate the coupling condition we present in Figure 7 for the 1D case the velocities \bar{v}_1 and v_1 as well as the negative stress $-\bar{\sigma}_{1,1}$ and the pressure in the elastic material and the gas, respectively. We note that the velocities as well as the negative stress and the pressure are continuous at the interface located at $x = 1 m$ confirming the coupling conditions (2.7).

4.2 2D Application

For the investigation of wave interactions at an interface separating an inviscid fluid and a linear elastic material we have performed 2D simulations for a single bubble near a solid surface, see Fig. 8. This can be considered a first step towards a more challenging problem of a single cavitation bubble in a liquid environment near a surface of a dynamically reacting, linear elastic solid to investigate the mechanism of cavitation damaging, see [11].

Computational setup. The bubble is a 2D-sphere with radius $r = 15$ mm separating hot gas at low pressure inside from surrounding cold gas at high pressure. The distance between the bubble origin and the solid surface is $d = 20$ mm. Again, the fluid is modeled by an ideal gas with the parameters

Elastic material				
	\bar{v}_1		$\bar{\sigma}_{11}$	
L	L_1 -error	EoC	L_1 -error	EoC
1	2.342E-03		5.331E+03	
2	1.418E-03	0.724	3.227E+03	0.724
3	8.263E-04	0.779	1.881E+03	0.779
4	4.717E-04	0.809	1.074E+03	0.809
5	2.704E-04	0.802	6.157E+02	0.802
6	1.562E-04	0.792	3.557E+02	0.792
7	9.065E-05	0.785	2.064E+02	0.785
8	5.270E-05	0.783	1.200E+02	0.783

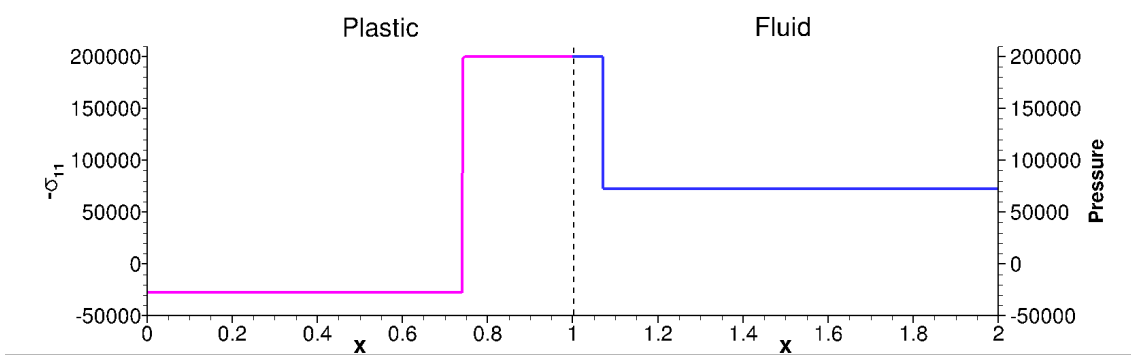
Table 2: Elastic material: error and empirical order of convergence (EoC) for 1D validation test case.

Fluid						
	ρ		v		p	
L	L_1 -error	EoC	L_1 -error	EoC	L_1 -error	EoC
1	7.021E-03		1.633E+03		5.010E+00	
2	3.738E-03	0.909	8.189E+02	0.996	2.445E+00	1.035
3	1.985E-03	0.913	4.450E+02	0.880	1.277E+00	0.937
4	1.002E-03	0.987	2.217E+02	1.005	6.725E-01	0.925
5	4.934E-04	1.021	1.065E+02	1.057	3.292E-01	1.030
6	2.499E-04	0.982	5.477E+01	0.960	1.637E-01	1.008
7	1.137E-04	1.136	2.388E+01	1.198	7.060E-02	1.214
8	6.497E-05	0.807	1.395E+01	0.776	3.878E-02	0.865

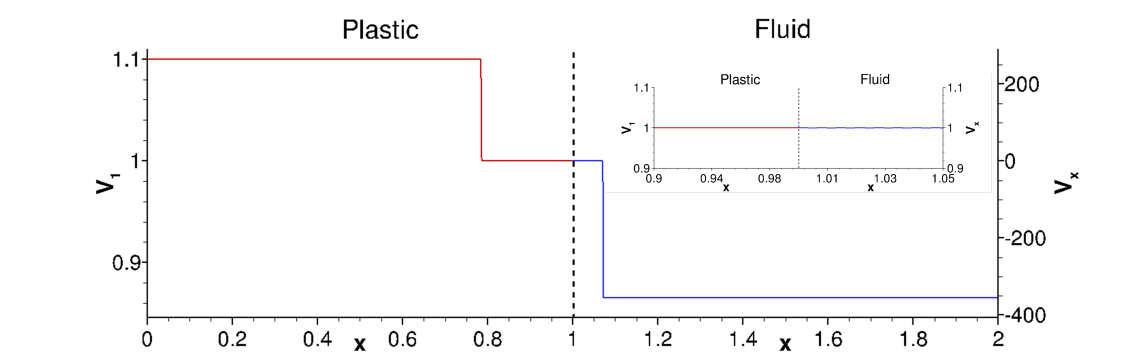
Table 3: Fluid: error and empirical order of convergence (EoC) for 1D validation test case.

given above. A high pressure gradient due to the gas pressure of 10^6 N/m² and 20×10^6 N/m² inside and outside the bubble, respectively, causes the collapse of the bubble. The temperatures of 293 K and 693 K correspond to a sound speed of about 343 m/s, and 528 m/s outside and inside the bubble, respectively. For the solid material we again choose plastic with material parameters given above. Initially we assume that the forces between the fluid and the adjacent structure are in equilibrium. Therefore we set the stress component orthogonal to the contact line identically to the cold gas pressure, i.e., $\sigma_{11} = -p$. All phases are supposed to be at rest. Note that the hot gas bubble does not come into contact with the interface. Otherwise the high temperature would cause material damage to the solid because it exceeds the melting point of plastics.

The computational domain consists of two parts $\Omega_s = [-0.22, 0] \times [0, 0.22]$ m² and $\Omega_f = [0, 0.11] \times [0, 0.22]$ m² for the solid and the fluid, respectively, that are connected at the contact line $\Gamma_s = \{0\} \times [0, 0.22]$. These domains are discretized each by 2×2 and 1×2 cells on the coarsest grid. The use of up to $L = 8$ refinement levels can lead to a resolution of $2 \cdot 2^L \times 2 \cdot 2^L = 1024 \times 1024$ cells and $1 \cdot 2^L \times 2 \cdot 2^L = 512 \times 1024$ cells for the solid grid and the flow grid, respectively. To reduce the computational load we perform the computation with local grid adaptation. During the computation the number of cells varies from 1243 (0.12%) to 134848 (12.9%) and 1430 (2.73%) to 28376 (5.41%) in the solid and the fluid, respectively, due to the evolving of waves and their interactions. Here the percentages in comparison to the fully refined grid are given in brackets. Both the fluid solver and the solid solver use the CFL number 0.025 from that determines the timestep used for both solvers to synchronize the time evolution. Since the wave speeds are larger in the elastic material and the spatial resolution is the same in both domains, the timestep size is



(a) Deformation and fluid velocity



(b) Negative normal stress and fluid pressure

Figure 7: 1D Riemann problem: velocity and pressure of fluid and deformation velocity and negative normal stress of elastic material. $L=12$.

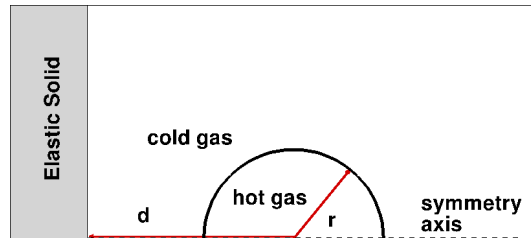


Figure 8: Configuration of a bubble next to an elastic solid.

typically dictated by the material rather than the fluid. We perform 51861 time steps to reach the final time $t = 0.00015$ s.

The computations were performed on the system 4 core Intel Core i7-3770, 3.4 GHz, 16 GB Ram. The computational time for the presented simulation was about 26.31 h. This large time consumption was caused by (i) the high resolution that requires small time steps due to the explicit time stepping and (ii) the fact that we have been using the same time step for both the fluid solver and the solid solver.

Wave dynamics in the fluid. The initial conditions correspond to a Riemann problem where three types of waves occur: an inward running compression shock followed by a contact discontinuity and an outward running rarefaction wave, see Figs. 10(a) and 9(a). The rarefaction wave and the shock wave are visible in the pressure, see Fig. 10, as well as in the density, see Fig. 9. Whereas the contact discontinuity is only seen in the density gradient profile.

The shock wave is focusing in the origin of the cold gas bubble. After the reflection in the center, the shock wave runs outward and passes the contact discontinuity. Hereby, the shock is partly

transmitted and partly reflected. The reflected part runs again into the center, is reflected and passes the contact discontinuity again, see Figs. 9 (a)-(e). By this process the hot gas bubble is shrinking and the state inside the bubble is compressed resulting in higher pressures and temperatures.

At time $t = 11.57\mu\text{s}$ the leading front of the rarefaction wave has reached the interface where it is reflected at the elastic material, see Figs. 9 (b), (c). There it is reflected as rarefaction. The corresponding doubling of the amplitude produces a region of low pressure which increases the shock pressure ratio and, therefore, accelerates the shock wave towards the wall, see Fig. 9 (d)-(f). The reflected rarefaction wave interacts with the reflected shock wave, see Figs. 9 (d)-(g). Since the sound speed is lower in the pre-shocked region than in the post-shocked region the reflected rarefaction wave is diffracted running faster in the post-shocked region.

At time $t = 69.42\mu\text{s}$ the outward running reflected shock wave starts interacting with the interface where it is reflected, see Figs. 9 (d), (e). The reflection area extends along the wall, see Fig. 9(f), developing a Mach stem, see Fig. 9(g). In the density contours the slip line, a contact discontinuity originating at the triple point of the Mach stem, is visible. The discontinuity separates two regions of different values of entropy that are caused in the material passing through shocks of different strength.

Wave dynamics in the linear elastic material. When the rarefaction wave impinges on the material interface in $\mathbf{x} = (0,0)$ at time $t = 11.57\mu\text{s}$ it is reflected into the fluid - as mentioned above - but by the coupling conditions it is also transmitted into the elastic material. In the material two waves develop, namely, the faster dilatation wave and the slower shear wave. Since both waves originate from the same point but move at different speeds another wave - the so-called von Schmidt wave develops connecting these two waves, see Figs. 9 (d), (e).

Since the wave speeds are about 5 times higher in the material than the sound speed in the fluid the transmitted wave propagates much faster in the material than the reflected rarefaction wave in the fluid, see Figs. 9 (b)-(g)

The same phenomena occurs when the shock wave impinges on the interface. The corresponding dilatation, shear and von Schmidt waves are clearly visible in Figs. 9 (e)-(g).

Coupling conditions. According to the coupling conditions (2.7) at the interface the velocity in the fluid and the deformation velocity in the material normal to the interface coincide and the fluid pressure equals the negative normal stress component in the material. To visualize these conditions we exemplarily show the pressure, see Fig. 10. Similar plots for velocity do not clearly exhibit the continuity at the interface because of the large difference in scales. Typically, the deformation velocity in the material is much smaller than the fluid velocity in interface normal direction and both differ by about two orders of magnitude. Therefore we do not show these pictures here.

5 Conclusion

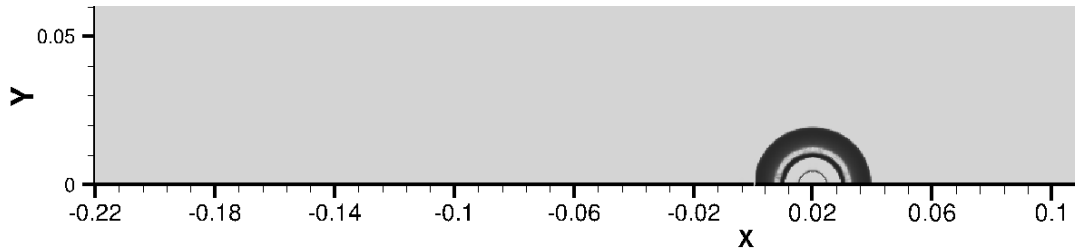
We presented a new coupling strategy for the simulation of fluid-structure interactions using a two-domain approach. This is motivated by recent work on coupling dynamics on networks. Here the novelty is to use an explicit approach rather an implicit approach that avoids costly nested iterations where the fluid solver and the solid solver are called alternately. We exemplify this concept for the coupling of a linear elastic structure with an ideal gas.

In each quadrature point at the coupling interface we solve a nonlinear scalar problem. We proved that there exists a unique solution to this problem under some constraints on the adjacent states in the solid and the fluid. In particular, the fluid state is assumed to be subsonic with respect to the velocity normal to the interface. During our computations we check these conditions but for all our computations they turned out to be satisfied.

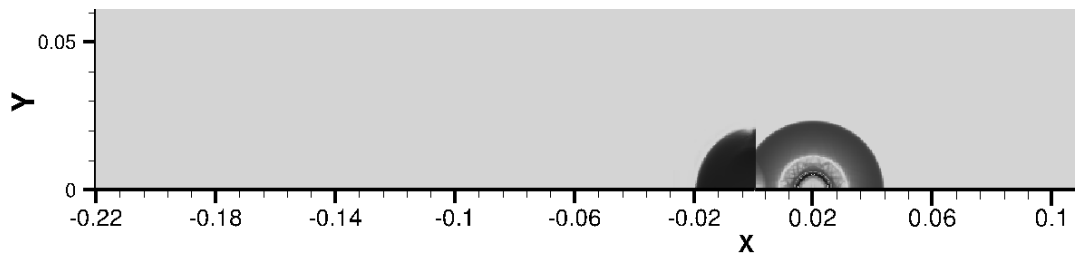
The coupling conditions and the implementation were validated by means of quasi-1D problems for which an explicit solution can be determined. For a more realistic scenario we considered a 2D application where a hot gas bubble at low pressure in a cold gas at high pressure collapses near a

structure. The resulting waves in the fluid interacted with the adjacent solid causing waves in the structure.

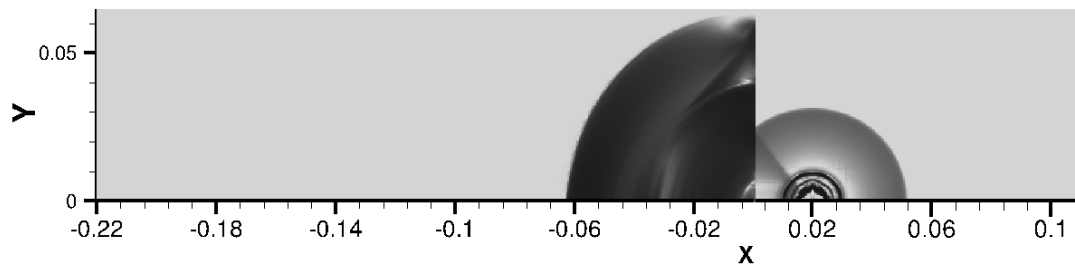
In future work we will extend our approach to two-phase fluids to investigate the material damage induced by collapsing cavitation bubbles near adjacent walls similar to [11] where only a second order discretization was used.



(a) $t = 11.57 \mu s$



(b) $t = 23.14 \mu s$



(c) $t = 46.29 \mu s$

Figure 9: 2D coupling: gradients of negative normal stress and fluid density. Coupling interface located at $x=0$.

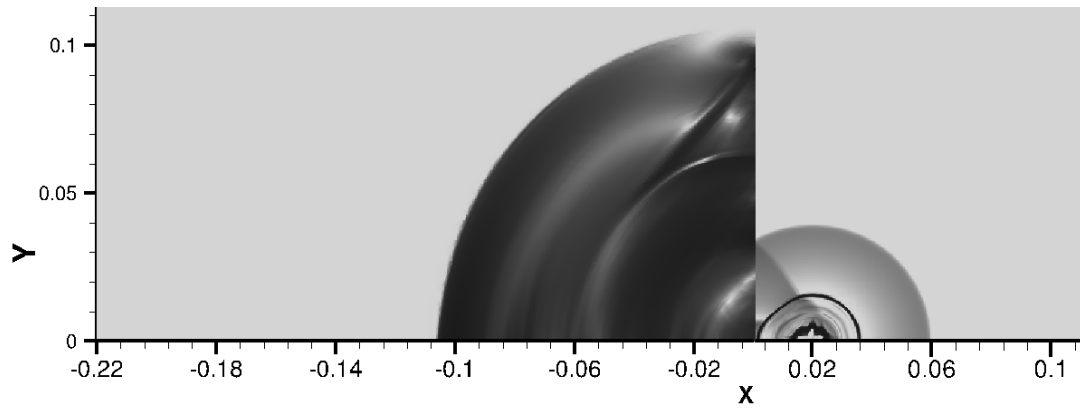
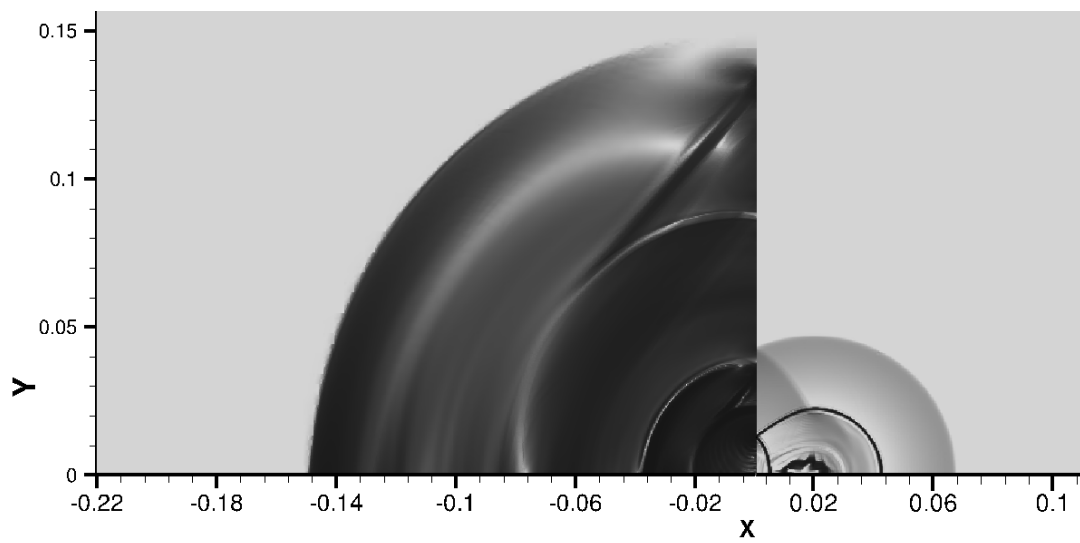
(d) $t = 69.42 \mu s$ (e) $t = 92.56 \mu s$

Figure 9: 2D coupling: gradients of negative normal stress and fluid density (continued). Coupling interface located at $x=0$.

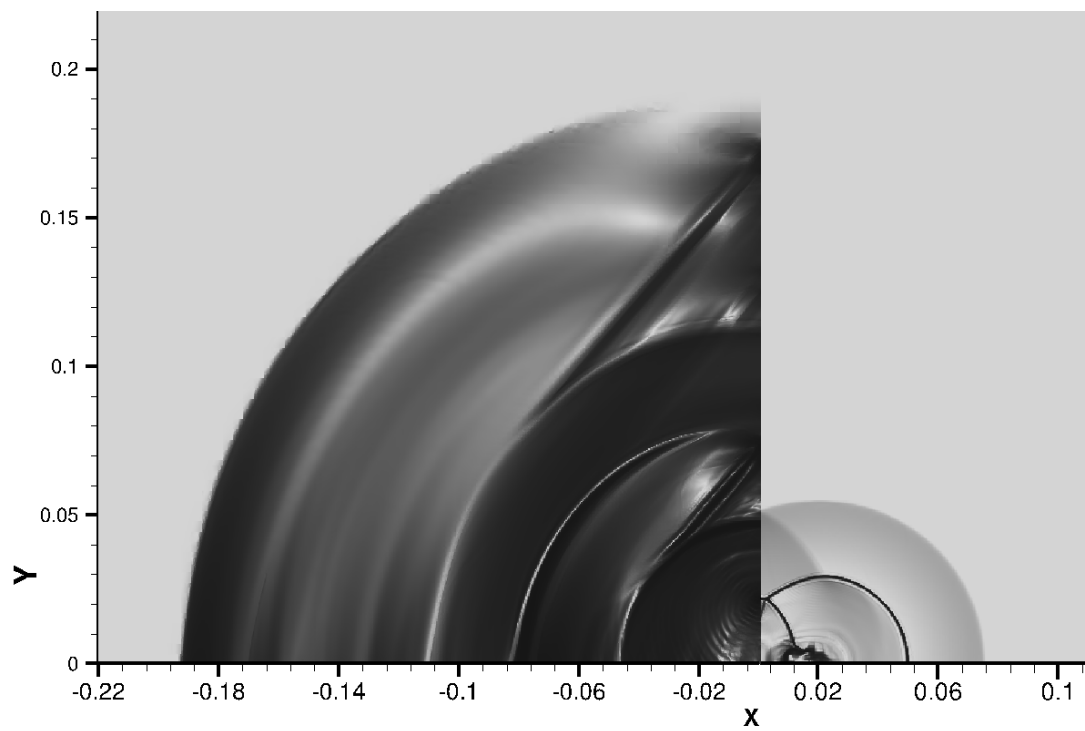
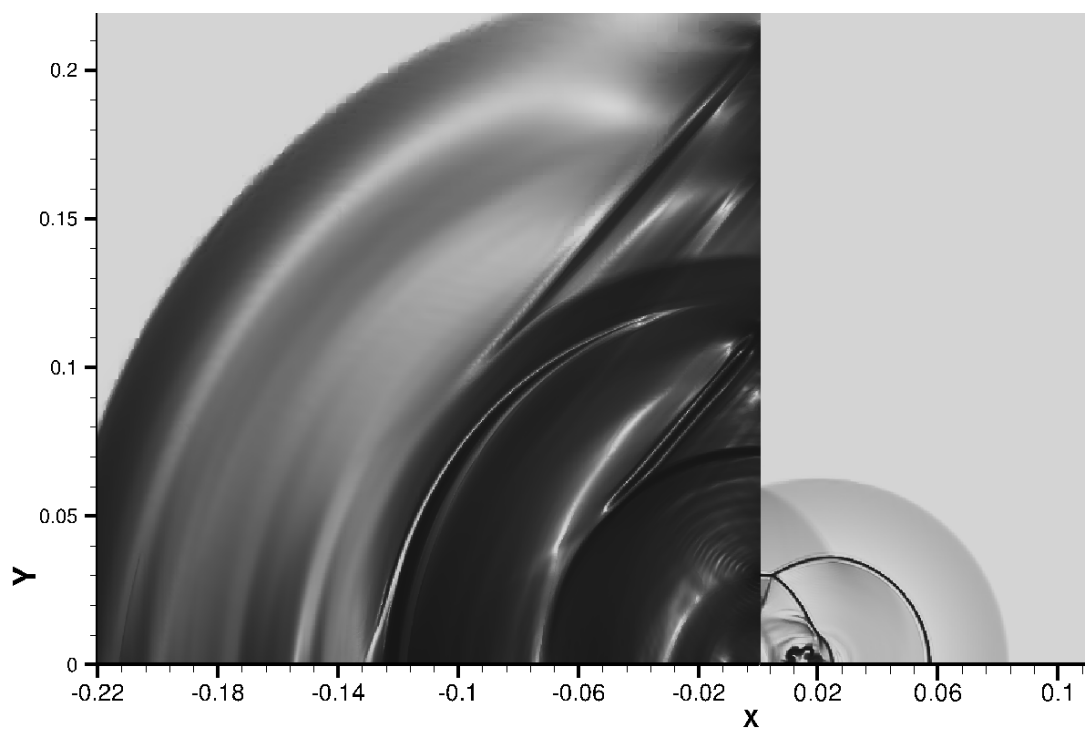
(f) $t = 115.69 \mu s$ (g) $t = 138.83 \mu s$

Figure 9: 2D coupling: gradients of negative normal stress and fluid density (continued). Coupling interface located at $x=0$.

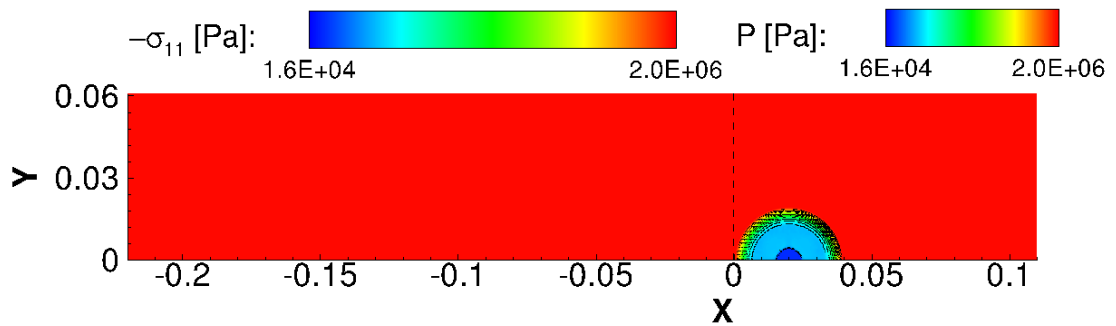
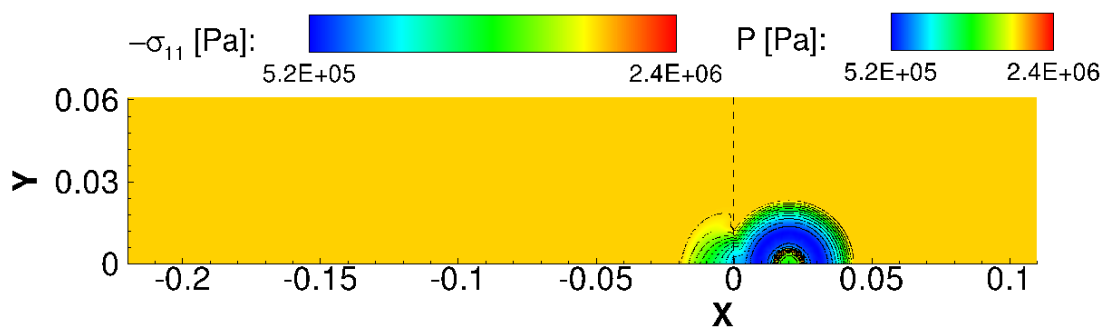
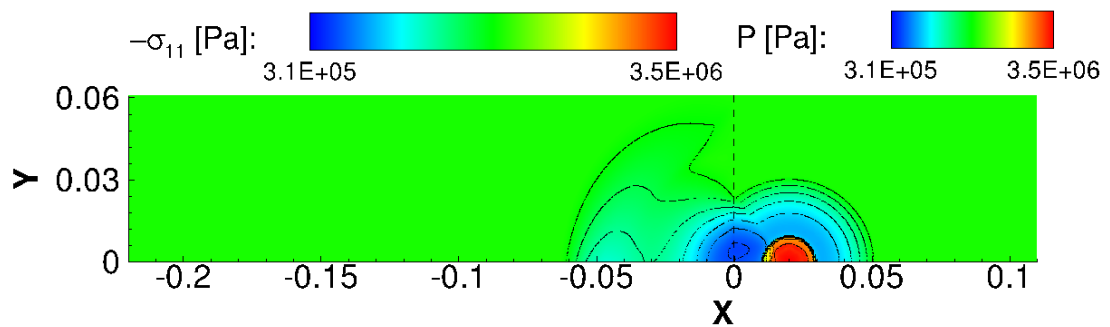
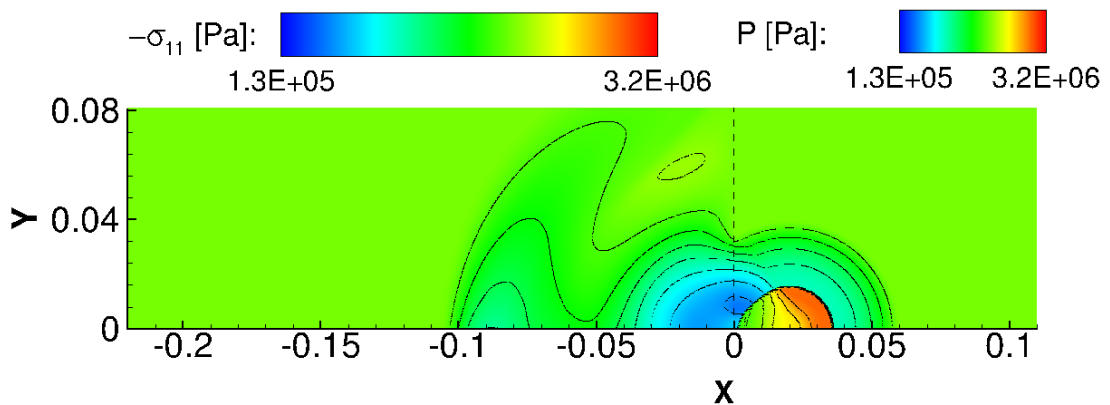
(a) $t = 11.57 \mu\text{s}$ (b) $t = 23.14 \mu\text{s}$ (c) $t = 46.29 \mu\text{s}$ (d) $t = 69.42 \mu\text{s}$

Figure 10: 2D coupling: contours of negative normal stress and fluid pressure. Dashed line indicates the coupling interface.

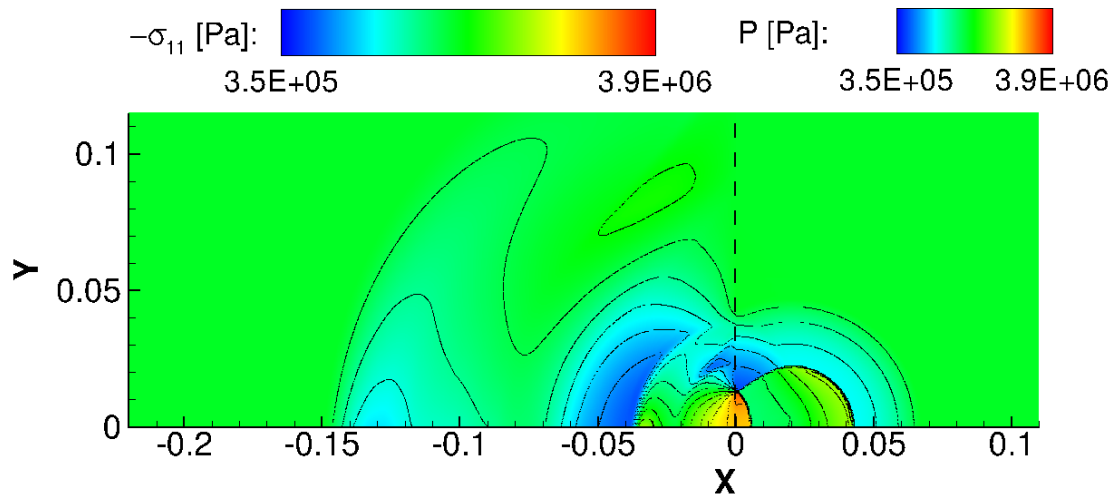
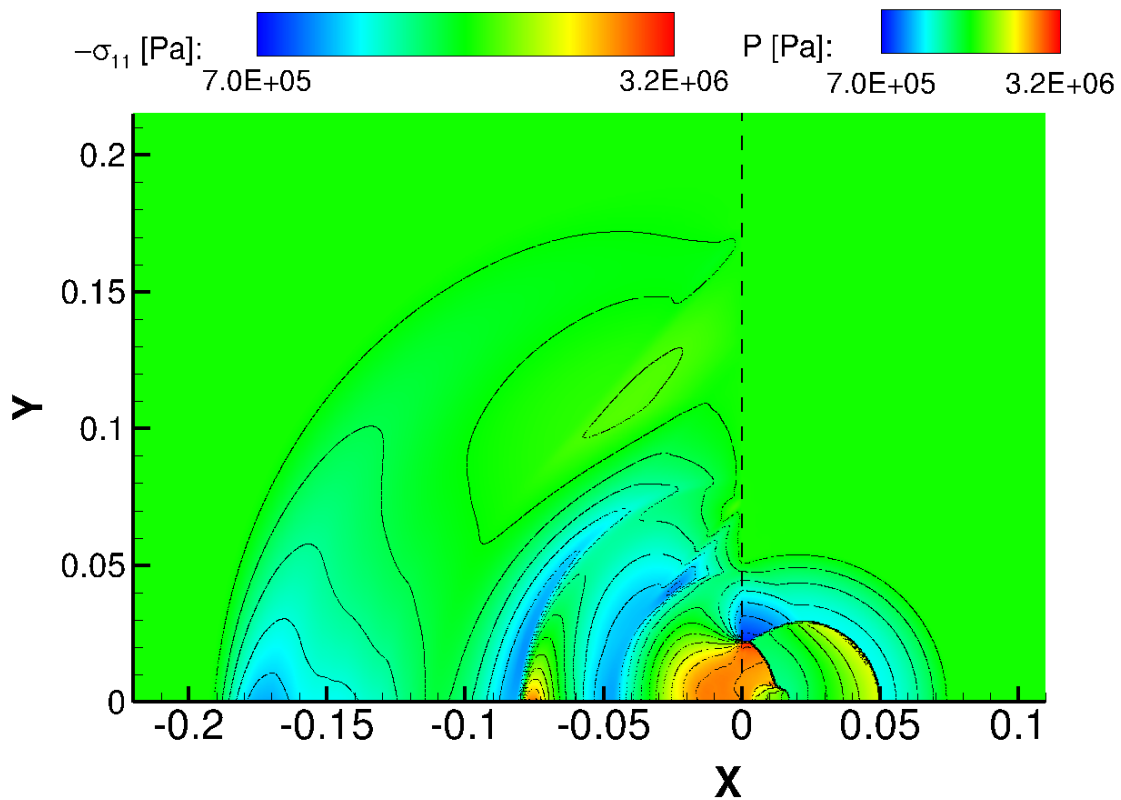
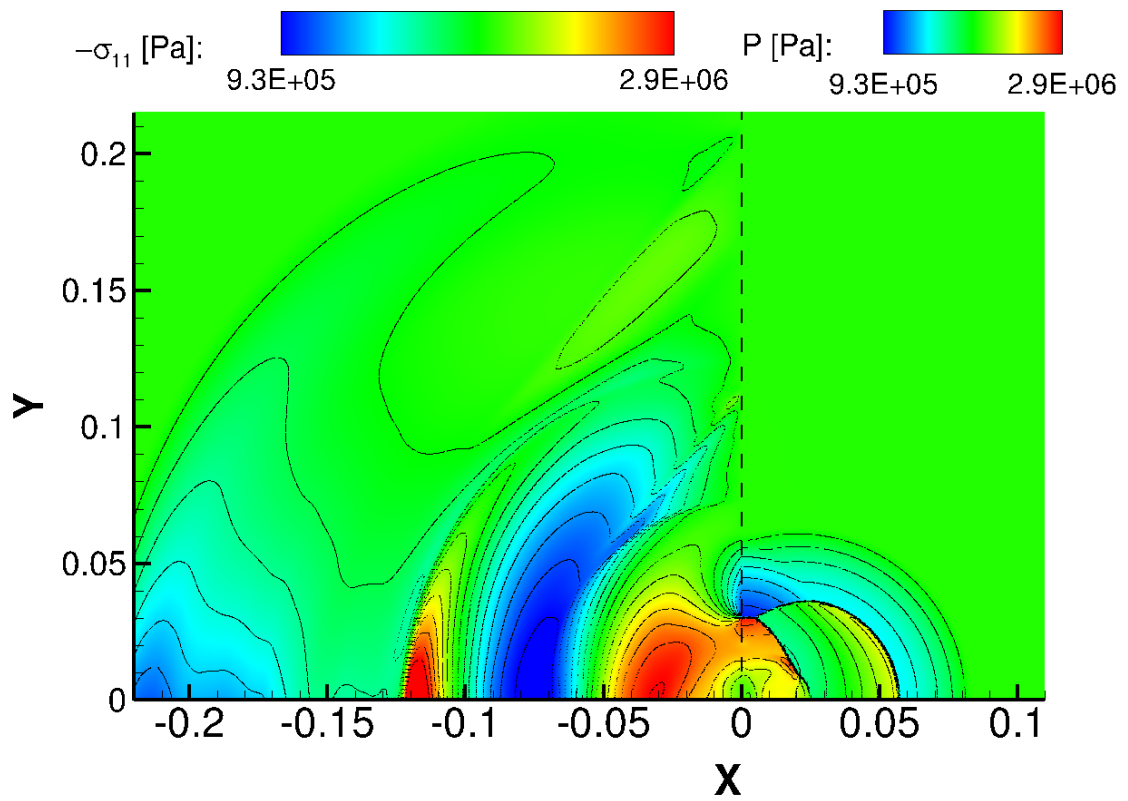
(e) $t = 92.56 \mu s$ (f) $t = 115.69 \mu s$

Figure 10: 2D coupling: contours of negative normal stress and fluid pressure (continued). Dashed line indicates the coupling interface.



(g) $t = 138.83 \mu s$

Figure 10: 2D coupling: contours of negative normal stress and fluid pressure (continued). Dashed line indicates the coupling interface.

Appendices

A Linear elastic model

Due to the symmetry of the stress tensor $\bar{\sigma}$, the system of equations (2.1) has redundant equations. Removing these redundant equations the system (2.1) can be written in the canonical form of a system of conservation laws

$$\frac{\partial \bar{\mathbf{u}}}{\partial t} + \nabla \cdot (\bar{\mathbf{f}}_1(\bar{\mathbf{u}}), \dots, \bar{\mathbf{f}}_d(\bar{\mathbf{u}})) = \mathbf{0} \quad (\text{A.1a})$$

$$\bar{\mathbf{u}} := (\bar{v}_1, \dots, \bar{v}_d, \bar{\sigma}_{11}, \dots, \bar{\sigma}_{1d}, \bar{\sigma}_{22}, \dots, \bar{\sigma}_{2d}, \dots, \bar{\sigma}_{d-1,d-1}, \dots, \bar{\sigma}_{d-1,d}, \bar{\sigma}_{d,d})^T \quad (\text{A.1b})$$

$$\bar{f}_{l,i}(\bar{\mathbf{u}}) = -\bar{\rho}^{-1} \bar{u}_{d+l+s_{d,i}}, \quad l = 1, \dots, d \quad (\text{A.1c})$$

$$\bar{f}_{l,d+j+s_{d,i}}(\bar{\mathbf{u}}) = -\bar{\lambda} \bar{u}_l \delta_{ij} - \bar{\mu} (\bar{u}_i \delta_{jl} + \bar{u}_j \delta_{il}), \quad j = i, \dots, d, i = 1, \dots, d \quad (\text{A.1d})$$

$$\text{mu with } s_{d,l} := \sum_{i=1}^{l-1} (d-i) = s_{d,l-1} + d - l + 1, \quad s_{d,1} := 0 \quad (\text{A.1e})$$

Since the system (2.1) is invariant under rotation/reflection, this holds true for the system (A.1a), i.e., it is equivalent to

$$\frac{\partial \tilde{\mathbf{u}}}{\partial t} + \nabla_{\tilde{\mathbf{x}}} \cdot (\tilde{\mathbf{f}}_1(\tilde{\mathbf{u}}), \dots, \tilde{\mathbf{f}}_d(\tilde{\mathbf{u}})) = \mathbf{0} \quad (\text{A.2})$$

under the transformation

$$\tilde{\mathbf{x}} := \mathbf{R}_d \mathbf{x}, \quad \mathbf{R}_d = (r_{ij})_{i,j=1,\dots,d} \in \mathbb{R}^{d \times d} \text{ (orthogonal matrix)} \quad (\text{A.3a})$$

$$\tilde{\mathbf{u}} := \mathbf{G}_d \mathbf{u}, \quad \mathbf{G}_d := \begin{pmatrix} \mathbf{R}_d & \mathbf{0} \\ \mathbf{0} & \mathbf{S}_d \end{pmatrix} \in \mathbb{R}^{(d+m_d) \times (d+m_d)}, \quad (\text{A.3b})$$

where the matrix $\mathbf{S}_d \in \mathbb{R}^{m_d \times m_d}$ with $m_d := \frac{d(d+3)}{2} - d$ is determined by the elements of \mathbf{R}_d . The matrices \mathbf{R}_d , \mathbf{S}_d and \mathbf{G}_d , respectively are needed in the implementation of the coupling conditions at an interface characterized by its local normal vector $\mathbf{n} \in \mathbb{R}^d$. For this purpose we give them here explicitly in terms of this normal vector. Then the columns of the orthogonal matrix \mathbf{R}_d are determined by the normal vector \mathbf{n} and the $d-1$ tangential vectors \mathbf{t}_i , $i = 1, \dots, d-1$, i.e., $\mathbf{R}_d = (\mathbf{n}, \mathbf{t}_1, \dots, \mathbf{t}_{d-1})$. For the dimensions $d = 1, 2, 3$ we then obtain:

Case 1: $d = 1$:

$$\mathbf{R}_1 = (1) = \mathbf{R}^{-1}, \quad \mathbf{S}_1 = (1) = \mathbf{S}^{-1} \quad (\text{A.4})$$

Case 2: $d = 2$:

$$\mathbf{R}_2 = \begin{pmatrix} n_1 & n_2 \\ -sn_2 & sn_1 \end{pmatrix} = (\mathbf{R}_2^{-1})^T, \quad n_1^2 + n_2^2 = 1, \quad s := \text{sgn}(n_1), \text{ if } n_1 \neq 0, \text{ else } s := 1 \quad (\text{A.5a})$$

$$\mathbf{S}_2 = \begin{pmatrix} r_{11}^2 & 2r_{11}r_{12} & r_{12}^2 \\ r_{11}r_{21} & r_{12}r_{21} + r_{11}r_{22} & r_{12}r_{22} \\ r_{21}^2 & 2r_{22}r_{21} & r_{22}^2 \end{pmatrix}, \quad \mathbf{S}_2^{-1} = \begin{pmatrix} r_{11}^2 & 2r_{11}r_{21} & r_{21}^2 \\ r_{11}r_{12} & r_{11}r_{22} + r_{21}r_{12} & r_{21}r_{22} \\ r_{12}^2 & 2r_{12}r_{22} & r_{22}^2 \end{pmatrix} \quad (\text{A.5b})$$

Case 3: $d=3$:

$$\mathbf{R}_3 = \begin{pmatrix} n_1 & n_2 & n_3 \\ -n_2 & n_1 + n_3^2/(n_1 + s) & -n_2 n_3/(n_1 + s) \\ -n_3 & -n_3 n_2/(n_1 + s) & n_1 + n_2^2/(n_1 + s) \end{pmatrix} = (\mathbf{R}_3^{-1})^T, \quad n_1^2 + n_2^2 + n_3^2 = 1, \quad (\text{A.6a})$$

$$\mathbf{S}_3 = \begin{pmatrix} r_{11}^2 & 2r_{11}r_{12} & 2r_{11}r_{13} & r_{12}^2 & 2r_{12}r_{13} & r_{13}^2 \\ r_{11}r_{21} & r_{12}r_{21} + r_{11}r_{22} & r_{13}r_{21} + r_{11}r_{23} & r_{12}r_{22} & r_{13}r_{22} + r_{12}r_{23} & r_{13}r_{23} \\ r_{11}r_{31} & r_{12}r_{31} + r_{11}r_{32} & r_{13}r_{31} + r_{11}r_{33} & r_{12}r_{32} & r_{13}r_{32} + r_{12}r_{33} & r_{13}r_{33} \\ r_{21}^2 & 2r_{22}r_{21} & 2r_{23}r_{21} & r_{22}^2 & 2r_{22}r_{23} & r_{23}^2 \\ r_{21}r_{31} & r_{22}r_{31} + r_{21}r_{32} & r_{23}r_{31} + r_{21}r_{33} & r_{22}r_{32} & r_{23}r_{32} + r_{22}r_{33} & r_{23}r_{33} \\ r_{31}^2 & 2r_{31}r_{32} & 2r_{31}r_{33} & r_{32}^2 & 2r_{32}r_{33} & r_{33}^2 \end{pmatrix}, \quad (\text{A.6b})$$

$$\mathbf{S}_3^{-1} = \begin{pmatrix} r_{11}^2 & 2r_{11}r_{21} & 2r_{11}r_{31} & r_{21}^2 & 2r_{21}r_{31} & r_{31}^2 \\ r_{11}r_{12} & r_{12}r_{21} + r_{11}r_{22} & r_{31}r_{12} + r_{11}r_{32} & r_{21}r_{22} & r_{31}r_{22} + r_{21}r_{32} & r_{31}r_{32} \\ r_{11}r_{13} & r_{21}r_{13} + r_{11}r_{23} & r_{31}r_{13} + r_{11}r_{33} & r_{21}r_{23} & r_{31}r_{23} + r_{21}r_{33} & r_{31}r_{33} \\ r_{12}^2 & 2r_{22}r_{12} & 2r_{32}r_{12} & r_{22}^2 & 2r_{22}r_{32} & r_{32}^2 \\ r_{12}r_{13} & r_{22}r_{13} + r_{12}r_{23} & r_{32}r_{13} + r_{12}r_{33} & r_{22}r_{23} & r_{32}r_{23} + r_{22}r_{33} & r_{32}r_{33} \\ r_{13}^2 & 2r_{13}r_{23} & 2r_{13}r_{33} & r_{23}^2 & 2r_{23}r_{33} & r_{33}^2 \end{pmatrix} \quad (\text{A.6c})$$

To derive the coupling conditions we need to determine the Lax curves corresponding to the projected system (2.5). Since this is a linear system, the k -th forward (+) and backward (−) Lax curve corresponding to the k th field emanating from the state $\bar{\mathbf{u}}$ are given by

$$\bar{\mathbf{L}}_k^\pm(\varepsilon; \bar{\mathbf{u}}) = \bar{\mathbf{u}} \pm (\varepsilon - \bar{\lambda}_k) \bar{\mathbf{r}}_k, \quad (\text{A.7})$$

where $\bar{\lambda}_k$ and $\bar{\mathbf{r}}_k$ denote the eigenvalue and the corresponding right eigenvector of the Jacobian of the normal flux (2.5b). For the corresponding eigenvalues we obtain:

Case 1: $d=1$:

$$\bar{\lambda}_{1,\pm} = \pm \bar{c}_1, \quad (\text{A.8})$$

Case 2: $d=2$:

$$\bar{\lambda}_{1,\pm} = \pm \bar{c}_1, \quad \bar{\lambda}_{2,\pm} = \pm \bar{c}_2, \quad \bar{\lambda}_0 = 0 \quad (\text{A.9})$$

Case 3: $d=3$:

$$\bar{\lambda}_{1,\pm} = \pm \bar{c}_1 \text{ (single root)}, \quad \bar{\lambda}_{2,\pm} = \pm \bar{c}_2 \text{ (double root)}, \quad \bar{\lambda}_0 = 0 \text{ (triple root)} \quad (\text{A.10})$$

Obviously, the eigenvalues are independent of the direction \mathbf{n} . Because of the rotational invariance the corresponding left and right eigenvectors, which are orthogonal to each other, are only given for the direction $\mathbf{n} = \mathbf{e}_1 \in \mathbb{R}^d$.

Case 1: $d=1$:

$$\bar{\mathbf{r}}_{1,\pm} = (1, \mp \bar{\rho} \bar{c}_1)^T \quad (\text{A.11a})$$

$$\bar{\mathbf{l}}_{1,\pm} = \frac{1}{2\bar{\rho} \bar{c}_1} (\bar{\rho} \bar{c}_1, \mp 1)^T \quad (\text{A.11b})$$

Case 1: $d = 2$:

$$\bar{\mathbf{r}}_{1,\pm} = \bar{\beta}(1, 0, \mp \bar{\rho}\bar{c}_1, 0, \mp \bar{\alpha}\bar{\rho}\bar{c}_1)^T, \quad \bar{\beta} := \bar{c}_1^2 - \bar{c}_2^2 > 0 \quad (\text{A.12a})$$

$$\bar{\mathbf{r}}_{2,\pm} = \bar{\beta}(0, 1, 0, \mp \bar{\rho}\bar{c}_2, 0)^T \quad (\text{A.12b})$$

$$\bar{\mathbf{r}}_0 = (0, 0, 0, 0, -1)^T \quad (\text{A.12c})$$

$$\bar{\mathbf{l}}_{1,\pm} = \frac{1}{2\bar{\rho}\bar{c}_1} \frac{1}{\bar{\beta}} (\bar{\rho}\bar{c}_1, 0, \mp 1, 0, 0)^T \quad (\text{A.12d})$$

$$\bar{\mathbf{l}}_{2,\pm} = \frac{1}{2\bar{\rho}\bar{c}_2} \frac{1}{\bar{\beta}} (0, \bar{\rho}\bar{c}_2, 0, \mp 1, 0)^T \quad (\text{A.12e})$$

$$\bar{\mathbf{l}}_0 = (0, 0, \bar{\alpha}, 0, -1)^T \quad (\text{A.12f})$$

Case 3: $d = 3$:

$$\bar{\mathbf{r}}_{1,\pm} = (\pm 1/\bar{\rho}\bar{c}_1, 0, 0, -1, 0, 0, -\bar{\alpha}, 0, -\bar{\alpha})^T \quad (\text{A.13a})$$

$$\bar{\mathbf{r}}_{2,\pm}^1 = (0, -1, 0, 0, \pm \bar{\rho}\bar{c}_2, 0, 0, 0, 0)^T \quad (\text{A.13b})$$

$$\bar{\mathbf{r}}_{2,\pm}^2 = (0, 0, -1, 0, 0, \pm \bar{\rho}\bar{c}_2, 0, 0, 0)^T \quad (\text{A.13c})$$

$$\bar{\mathbf{r}}_0^1 = (0, 0, 0, 0, 0, 0, -2, 0, -1)^T \quad (\text{A.13d})$$

$$\bar{\mathbf{r}}_0^2 = (0, 0, 0, 0, 0, 0, 0, -1, 0)^T \quad (\text{A.13e})$$

$$\bar{\mathbf{r}}_0^3 = (0, 0, 0, 0, 0, 0, -1, 0, -1)^T \quad (\text{A.13f})$$

$$\bar{\mathbf{l}}_{1,\pm} = \frac{1}{2} (\pm \bar{\rho}\bar{c}_1, 0, 0, -1, 0, 0, 0, 0, 0)^T \quad (\text{A.13g})$$

$$\bar{\mathbf{l}}_{2,\pm}^1 = \frac{1}{2} (0, -1, 0, 0, \pm 1/\bar{\rho}\bar{c}_2, 0, 0, 0, 0)^T \quad (\text{A.13h})$$

$$\bar{\mathbf{l}}_{2,\pm}^2 = \frac{1}{2} (0, 0, -1, 0, 0, \pm 1/\bar{\rho}\bar{c}_2, 0, 0, 0)^T \quad (\text{A.13i})$$

$$\bar{\mathbf{l}}_0^1 = (0, 0, 0, 0, 0, 0, -1, 0, 1)^T \quad (\text{A.13j})$$

$$\bar{\mathbf{l}}_0^2 = (0, 0, 0, 0, 0, 0, -1, 0, 0)^T \quad (\text{A.13k})$$

$$\bar{\mathbf{l}}_0^3 = (0, 0, 0, \bar{\alpha}, 0, 0, 1, 0, -2)^T \quad (\text{A.13l})$$

The coupling states on the forward Lax–curves for the linear elastic system are

$$\bar{\mathbf{u}}_1 = \bar{\mathbf{u}}_L + (\bar{\xi}_1^+ - \bar{\lambda}_{1,-}) \bar{\mathbf{r}}_{1,-} \quad (d=1) \quad (\text{A.14a})$$

$$\bar{\mathbf{u}}_2 = \bar{\mathbf{u}}_L + (\bar{\xi}_1^+ - \bar{\lambda}_{1,-}) \bar{\mathbf{r}}_{1,-} + (\bar{\xi}_2^+ - \bar{\lambda}_{2,-}) \bar{\mathbf{r}}_{2,-} \quad (d=2) \quad (\text{A.14b})$$

$$\bar{\mathbf{u}}_2 = \bar{\mathbf{u}}_L + (\bar{\xi}_1^+ - \bar{\lambda}_{1,-}) \bar{\mathbf{r}}_{1,-} + (\bar{\xi}_2^+ - \bar{\lambda}_{2,-}) \bar{\mathbf{r}}_{2,-}^1 + (\bar{\xi}_3^+ - \bar{\lambda}_{2,-}) \bar{\mathbf{r}}_{2,-}^2 \quad (d=3) \quad (\text{A.14c})$$

B Euler equations

Introducing the vector $\mathbf{u} = (\rho, \rho \mathbf{v}^T, \rho E)^T$ of conserved quantities and the fluxes \mathbf{f}_i , $i = 1, \dots, d$, we can rewrite the Euler equations (2.2) in analogy to (A.1) in the form

$$\frac{\partial \mathbf{u}}{\partial t} + \nabla \cdot (\mathbf{f}_1(\mathbf{u}), \dots, \mathbf{f}_d(\mathbf{u})) = \mathbf{0}. \quad (\text{B.1a})$$

$$\mathbf{f}_i(\mathbf{u}) = (\rho v_i, \rho v_i \mathbf{v}^T + p \mathbf{e}_i^T, \rho v_i (E + p/\rho))^T. \quad (\text{B.1b})$$

Because of rotational invariance this system is equivalent to

$$\frac{\partial \tilde{\mathbf{u}}}{\partial t} + \nabla_{\tilde{\mathbf{x}}} \cdot (\mathbf{f}_1(\tilde{\mathbf{u}}), \dots, \mathbf{f}_d(\tilde{\mathbf{u}})) = \mathbf{0} \quad (\text{B.2})$$

under the orthogonal transformation

$$\tilde{\mathbf{x}} := \mathbf{R}\mathbf{x}, \quad \tilde{\mathbf{u}} := \bar{\mathbf{R}}\mathbf{u} = \begin{pmatrix} \rho \\ \rho \tilde{\mathbf{v}} \\ \rho E \end{pmatrix}, \quad \tilde{\mathbf{v}} := \mathbf{R}\mathbf{v} \quad (\text{B.3})$$

with

$$\bar{\mathbf{R}} := \begin{pmatrix} 1 & \mathbf{0}^T & 0 \\ \mathbf{0} & \mathbf{R} & \mathbf{0} \\ 0 & \mathbf{0}^T & 1 \end{pmatrix}, \quad \mathbf{R} = (\mathbf{r}_1, \dots, \mathbf{r}_d)^T \in \mathbb{R}^{d \times d} \text{ orthogonal}, \quad (\text{B.4})$$

To determine the coupling conditions at an interface locally characterized by the normal vector $\mathbf{n} \in \mathbb{R}^d$ we need the flow in this normal direction. For this purpose we project the system (B.1) onto direction \mathbf{n} . The quasi-1D projected system can be derived from (B.2) where we choose $\mathbf{R}^T = (\mathbf{n}, \mathbf{t}_1, \dots, \mathbf{t}_{d-1}) = (\mathbf{r}_1, \dots, \mathbf{r}_d)$. Assuming no flow in tangential directions $\tilde{x}_{i+1} = \mathbf{x} \cdot \mathbf{t}_i$, $i = 1, \dots, d-1$, then the system (B.2) reduces to the projected system (2.6). The corresponding eigenvalues to the projected system (2.6) are determined by

$$\lambda_{\pm} = v_n \pm c, \quad \lambda_0 = v_n \quad (d\text{-multiple}) \quad (\text{B.5})$$

with right and left eigenvectors that are orthogonal to each other

$$\mathbf{r}_{\pm} = \begin{pmatrix} 1 \\ \mathbf{v} \pm c\mathbf{n} \\ H \pm cv_n \end{pmatrix}, \quad \mathbf{r}_0^1 = \begin{pmatrix} 1 \\ \mathbf{v} \\ \frac{1}{2}\mathbf{v}^2 \end{pmatrix}, \quad \mathbf{r}_0^{i+1} = \begin{pmatrix} 0 \\ c\mathbf{t}_i \\ c\mathbf{v} \cdot \mathbf{t}_i \end{pmatrix}, \quad i = 1, \dots, d-1 \quad (\text{B.6a})$$

$$\mathbf{l}_{\pm} = \frac{1}{c^2} \begin{pmatrix} \frac{1}{2}(\frac{1}{2}\bar{\kappa}\mathbf{v}^2 \mp cv_n) \\ \pm \frac{1}{2}(c\mathbf{n} + \bar{\kappa}\mathbf{v}) \\ \frac{1}{2}\bar{\kappa} \end{pmatrix}, \quad \mathbf{l}_0^1 = \frac{1}{c^2} \begin{pmatrix} c^2 - \frac{1}{2}\bar{\kappa}\mathbf{v}^2 \\ \bar{\kappa}\mathbf{v} \\ -\bar{\kappa} \end{pmatrix}, \quad \mathbf{l}_0^{i+1} = \frac{1}{c^2} \begin{pmatrix} -c\mathbf{v} \cdot \mathbf{t}_i \\ c\mathbf{t}_i \\ 0 \end{pmatrix}, \quad i = 1, \dots, d-1. \quad (\text{B.6b})$$

Here $H := E + p/\rho$ denotes the total enthalpy and $\bar{\kappa} = \gamma - 1$.

For $d \geq 2$ the tangential velocity components do not change neither along a rarefaction curve nor a shock curve, but may jump arbitrarily on a contact curve. On the other hand, across a contact discontinuity the pressure and the normal velocity and the normal momentum, respectively, are continuous whereas the tangential velocities and momentum may jump arbitrarily. Therefore, we may solve the Riemann problem to the projected system (2.6) as in the one-dimensional case for ρ , ρv_n and ρE and then setting the tangential velocity components to their initial values to either side of the contact discontinuity.

To derive the coupling conditions we need to determine the Lax curves corresponding to the projected system (2.6). As mentioned before it will be sufficient to consider the one-dimensional

case only where $v_n = v_1 = v$. According to [9] the Lax curves can be parameterized by a shift of the density ρ . The forward (+)/backward (-) Lax curves L_i^\pm emanating from the state $\mathbf{u}_0 = (\rho_0, (\rho v)_0, (\rho E)_0)$ are given by

$$L_i^\pm(\sigma; \mathbf{u}_0) = \begin{cases} S_i^\pm(\sigma; \mathbf{u}_0) & \text{if } \sigma \leq 0 \\ R_i^\pm(\sigma; \mathbf{u}_0) & \text{if } \sigma \geq 0 \end{cases}, \quad i=1,3. \quad (\text{B.7})$$

In case of a perfect gas the forward (+)/backward (-) shock curve S_i^\pm and rarefaction curve R_i^\pm read

$$S_i^\pm(\sigma; \mathbf{u}_0) = \begin{cases} \rho = \pm(i-2)\sigma + \rho_0 \\ v = v_0 \mp \sqrt{\frac{2\gamma(\gamma-1)e_0\sigma^2}{(2\rho_0 \pm (2-i)(\gamma-1)\sigma)(\rho_0 \pm (i-2)\sigma)}} \\ e = \frac{1}{1 \pm (i-2)\sigma/\rho_0} \frac{2 \pm (i-2)(\gamma+1)\sigma/\rho_0}{2 \pm (2-i)(\gamma-1)\sigma/\rho_0} e_0 \end{cases}, \quad i=1,3 \quad (\text{B.8a})$$

$$R_i^\pm(\sigma; \mathbf{u}_0) = \begin{cases} \rho = \pm(i-2)\sigma + \rho_0 \\ v = v_0 + (2-i)2\sqrt{\frac{\gamma}{\gamma-1}} \left(1 - \left(1 \pm (i-2)\frac{\sigma}{\rho_0}\right)^{(\gamma-1)/2}\right) \sqrt{e_0} \\ s = s_0 \end{cases}, \quad i=1,3 \quad (\text{B.8b})$$

Here s denotes the entropy that for a perfect gas is given by

$$s(\rho, e) = c_v(\ln e - (\gamma-1)\ln \rho) \quad (\text{B.9})$$

or, equivalently,

$$e(\rho, s) = \exp(s/c_v + (\gamma-1)\ln \rho), \quad \gamma > 1 \quad (\text{B.10})$$

where γ denotes the ratio of specific heats at constant pressure and volume, respectively. In particular, in case of a perfect gas it holds

$$\gamma = \frac{c_p}{c_v} = 1 + \frac{R}{c_v} \quad (\text{B.11})$$

with R the specific gas constant.

For sake of completeness we give also the forward/backward Lax curve for the contact wave:

$$L_2^\pm(\sigma; \mathbf{u}_0) = \begin{cases} \rho = \rho_0 \pm \sigma \\ v = v_0 \\ p = p_0 \end{cases}. \quad (\text{B.12})$$

Here the velocity and the pressure remain unchanged whereas the density varies linearly across the contact discontinuity that corresponds to a linearly degenerated field. Note that in the multi-dimensional case there are additional $d-1$ contact discontinuities where only the tangential velocity corresponding to the tangent vector \mathbf{t}_i , $i=1, \dots, d-1$, varies linearly, i.e.,

$$L_{2,i}^\pm(\sigma; \mathbf{u}_0) = \begin{cases} \rho = \rho_0 \\ v_n = \mathbf{n} \cdot \mathbf{v}_0 \\ v_{t_i} = \mathbf{t}_i \cdot \mathbf{v}_0 \pm \sigma \\ v_{t_j} = \mathbf{t}_j \cdot \mathbf{v}_0, \quad j \neq i \\ p = p_0 \end{cases}. \quad (\text{B.13})$$

In the subsonic case the coupling states on the backward Lax–curves are given by

$$\mathbf{u}_2 = \mathbf{L}_3^-(\varepsilon_3; \mathbf{u}_3) \quad (\text{B.14})$$

for the case 1a scenario and

$$\mathbf{u}_2 = \mathbf{L}_3^-(\varepsilon_3; \mathbf{u}_3), \quad (\text{B.15a})$$

$$\mathbf{u}_1 = \mathbf{L}_2^-(\varepsilon_2; \mathbf{u}_2) = \mathbf{L}_2^-(\varepsilon_2; \mathbf{L}_3^-(\varepsilon_3; \mathbf{u}_R)) \quad (\text{B.15b})$$

for the case 1b scenario, respectively. Since the pressure p and the normal velocity v_n are continuous across the contact discontinuity we obtain the same states for both cases, i.e.,

$$\begin{pmatrix} p \\ v_n \end{pmatrix} = \begin{pmatrix} p_3^-(\varepsilon_3, \mathbf{u}_R) \\ (v_n)_3^-(\varepsilon_3, \mathbf{u}_R) \end{pmatrix}. \quad (\text{B.16})$$

Acknowledgments

This work has been supported in part by the German Research Council (DFG) within the DFG Collaborative Research Center SFB-TR-40, TP A1, and by KI-Net NSF RNMS grant No. 1107444, grants DFG Cluster of Excellence 'Production technologies for high-wage countries', HE5386/13,14,15-1, DAAD–MIUR project. The authors Gaoming Xiang and Bing Wang would like to thank for financial support from the National Natural Science Foundation of China (No. 51676111).

References

- [1] ADIMURTHI, S. MISHRA, AND G. VEERAPPA GOWDA, *Optimal entropy solutions for conservation laws with discontinuous flux-functions.*, J. Hyperbolic Differ. Equ., 2 (2005), pp. 783–837.
- [2] J. BALLMANN, ed., *Flow modulation and fluid-structure interaction at airplane wings.*, vol. 84 of Notes on Numerical Fluid Mechanics and Multidisciplinary Design, Berlin: Springer, 2003.
- [3] M. K. BANDA, A. HAECK, AND M. HERTY, *Numerical discretization of coupling conditions by high-order schemes*, Journal of Scientific Computing, (2016).
- [4] M. K. BANDA, M. HERTY, AND A. KLAR, *Gas flow in pipeline networks*, Netw. Heterog. Media, 1 (2006), pp. 41–56.
- [5] Y. BAZILEVS, K. TAKIZAWA, AND T. E. TEZDUYAR, *Computational Fluid-Structure Interaction: Methods and Applications*, Wiley Series in Computational Mechanics, John Wiley & Sons Ltd, 2013.
- [6] A. BRESSAN, S. CANIC, M. GARAVELLO, M. HERTY, AND B. PICCOLI, *Flow on networks: recent results and perspectives*, European Mathematical Society-Surveys in Mathematical Sciences, 1 (2014), pp. 47–11.
- [7] B. COCKBURN AND C.-W. SHU, *The Runge-Kutta discontinuous Galerkin method for conservation laws V: Multidimensional systems*, J. Comput. Phys., 141 (1998), pp. 199–244.
- [8] R. M. COLOMBO, G. GUERRA, M. HERTY, AND V. SCHLEPER, *Optimal control in networks of pipes and canals*, SIAM J. Control Optim., 48 (2009), pp. 2032–2050.
- [9] R. M. COLOMBO AND C. MAURI, *Euler system at a junction*, Journal of Hyperbolic Differential Equations, 5 (2007), pp. 547–568.
- [10] C. M. DAFERMOS, *Hyperbolic conservation laws in continuum physics*, vol. 325 of Grundlehren der Mathematischen Wissenschaften [Fundamental Principles of Mathematical Sciences], Springer-Verlag, Berlin, second ed., 2005.
- [11] C. DICKOPP, R. GARTZ, AND S. MÜLLER, *Coupling of elastic solids with compressible two-phase fluids for the numerical investigation of cavitation damaging.*, International Journal on Finite Volumes, 10 (2013), pp. 1–39. hal-01121991.
- [12] N. GERHARD, F. IACONO, G. MAY, S. MÜLLER, AND R. SCHÄFER, *A high-order discontinuous Galerkin discretization with multiwavelet-based grid adaptation for compressible flows.*, J. Sci. Comput., 62 (2015), pp. 25–52.
- [13] N. GERHARD AND S. MÜLLER, *Adaptive multiresolution discontinuous Galerkin schemes for conservation laws: multi-dimensional case.*, Comp. Appl. Math., 35 (2016), pp. 321–349.

- [14] E. GODLEWSKI, K.-C. LE THANH, AND P.-A. RAVIART, *The numerical interface coupling of nonlinear hyperbolic systems of conservation laws. II. The case of systems*, M2AN Math. Model. Numer. Anal., 39 (2005), pp. 649–692.
- [15] E. GODLEWSKI AND P.-A. RAVIART, *The numerical interface coupling of nonlinear hyperbolic systems of conservation laws. I. The scalar case*, Numer. Math., 97 (2004), pp. 81–130.
- [16] E. GODLEWSKI AND P. A. RAVIART, *A method of coupling non-linear hyperbolic systems: examples in CFD and plasma physics*, Internat. J. Numer. Methods Fluids, 47 (2005), pp. 1035–1041. 8th ICFD Conference on Numerical Methods for Fluid Dynamics. Part 2.
- [17] M. HERTY, M. SEAÏD, AND A. K. SINGH, *A domain decomposition method for conservation laws with discontinuous flux function*, Appl. Numer. Math., 57 (2007), pp. 361–373.
- [18] G. HOU, J. WANG, AND A. LAYTON, *Numerical methods for fluid-structure interaction - a review*, Commun. Comput. Phys., 12 (2012), pp. 337–377.
- [19] N. HOVHANNISYAN, S. MÜLLER, AND R. SCHÄFER, *Adaptive Multiresolution Discontinuous Galerkin Schemes for Conservation Laws.*, Math. Comput., 83 (2014), pp. 113–151.
- [20] R. MENIKOFF AND B. PLOHR, *The Riemann problem for fluid flows of real materials*, Rev. Mod. Phys., 61 (1989), pp. 75–130.
- [21] W. SCHRÖDER, ed., *Summary of Flow Modulation and Fluid-Structure Interaction Findings.*, vol. 109 of Notes on Numerical Fluid Mechanics and Multidisciplinary Design, Berlin: Springer, 2010.